

1 MusMorph, a database of standardized mouse morphology data for 2 morphometric meta-analyses

3 November 10, 2021

4 Jay Devine^{1,2,3}, Marta Vidal-García^{1,2,3}, Wei Liu^{1,2,3}, Amanda Neves⁴, Lucas D. Lo Vercio^{1,2,3},
5 Rebecca M. Green⁵, Heather A. Richbourg⁶, Marta Marchini^{1,2,3}, Colton M. Unger^{2,7}, Audrey C.
6 Nickle^{8,9}, Bethany Radford^{1,10}, Nathan M. Young⁶, Paula N. Gonzalez¹¹, Robert E. Schuler¹²,
7 Alejandro Bugacov¹², Campbell Rolian^{2,13}, Christopher J. Percival¹⁴, Trevor Williams¹⁵, Lee
8 Niswander¹⁶, Anne L. Calof^{17,18}, Arthur D. Lander^{17,34}, Axel Visel^{19,20,33}, Frank R. Jirik^{1,2,10},
9 James M. Cheverud²², Ophir Klein^{23,24}, Ramon Y. Birnbaum²⁵, Amy E. Merrill^{8,9}, Rebecca R.
10 Ackermann^{26,27}, Daniel Graf^{28,29}, Myriam Hemberger^{1,10}, Wendy Dean^{1,10}, Nils D. Forkert^{1,30},
11 Stephen A. Murray³¹, Henrik Westerberg³², Ralph S. Marcucio⁶, Benedikt Hallgrímsson^{1,2,3}

- 12 1. Alberta Children's Hospital Research Institute, University of Calgary, Calgary, AB, CANADA
- 13 2. The McCaig Institute for Bone and Joint Health, University of Calgary, Calgary, AB, CANADA
- 14 3. Department of Cell Biology and Anatomy, Cumming School of Medicine, University of Calgary, Calgary, AB, CANADA
- 15 4. Department of Biology, McMaster University, Hamilton, ON, CANADA
- 16 5. School of Dental Medicine, University of Pittsburgh, Pittsburgh, PA, USA
- 17 6. Department of Orthopedics, University of California, San Francisco, San Francisco, CA, USA
- 18 7. Department of Biological Sciences, University of Calgary, Calgary, AB, CANADA
- 19 8. Center for Craniofacial Molecular Biology, Herman Ostrow School of Dentistry, University of Southern California, Los Angeles, CA, USA
- 20 9. Department of Biochemistry and Molecular Medicine, Keck School of Medicine, University of Southern California, Los Angeles, CA, USA
- 21 10. Department of Biochemistry and Molecular Biology, Cumming School of Medicine, University of Calgary, Calgary, AB, CANADA
- 22 11. Institute for Studies in Neuroscience and Complex Systems (ENyS) CONICET, Buenos Aires, ARGENTINA
- 23 12. Information Sciences Institute, Viterbi School of Engineering, University of Southern California, Marina del Rey, CA, USA
- 24 13. Department of Comparative Biology and Experimental Medicine, Faculty of Veterinary Medicine, University of Calgary, Calgary, AB, CANADA
- 25 14. Department of Anthropology, Stony Brook University, New York, NY, USA
- 26 15. Department of Craniofacial Biology, University of Colorado, Aurora, CO, USA
- 27 16. Department of Molecular, Cellular and Developmental Biology, University of Colorado Boulder, Boulder, CO, USA
- 28 17. Department of Anatomy and Neurobiology, University of California, Irvine, Irvine, CA, USA
- 29 18. Center for Complex Biological Systems, University of California, Irvine, Irvine, CA, USA
- 30 19. Environmental Genomics and Systems Biology Division, Lawrence Berkeley National Laboratory, Berkeley, CA, USA
- 31 20. U.S. Department of Energy Joint Genome Institute, Lawrence Berkeley National Laboratory, Berkeley, CA, USA
- 32 21. Department of Biochemistry and Molecular Biology, Cumming School of Medicine, University of Calgary, Calgary, AB, CANADA
- 33 22. Department of Biology, Loyola University Chicago, Chicago, IL, USA
- 34 23. Program in Craniofacial Biology and Department of Orofacial Sciences, University of California, San Francisco, San Francisco, CA, USA
- 35 24. Department of Pediatrics and Institute for Human Genetics, University of California, San Francisco, San Francisco, CA, USA
- 36 25. Department of Life Sciences, Faculty of Natural Sciences, The Ben-Gurion University of the Negev, Beer-Sheva, ISRAEL
- 37 26. Department of Archaeology, University of Cape Town, Cape Town, Rondebosch, SOUTH AFRICA
- 38 27. Human Evolution Research Institute, University of Cape Town, Cape Town, Rondebosch, SOUTH AFRICA
- 39 28. School of Dentistry, Faculty of Medicine and Dentistry, University of Alberta, Edmonton, AB, CANADA
- 40 29. Department of Medical Genetics, Faculty of Medicine and Dentistry, University of Alberta, Edmonton, AB, CANADA
- 41 30. Department of Radiology, Cumming School of Medicine, University of Calgary, Calgary, AB, CANADA
- 42 31. The Jackson Laboratory, Bar Harbor, ME, USA
- 43 32. Department of Bioimaging Informatics, MRC Harwell Institute, Oxfordshire, UK
- 44 33. School of Natural Sciences, University of California, Merced, Merced, CA, USA
- 45 34. Department of Developmental and Cell Biology, University of California, Irvine, CA, USA

51
52 Corresponding author: Benedikt Hallgrímsson (bhallgri@ucalgary.ca)

53

54

55 Abstract

56 Complex morphological traits are the product of many genes with transient or lasting developmental effects
57 that interact in anatomical context. Mouse models are a key resource for disentangling such effects, because
58 they offer myriad tools for manipulating the genome in a controlled environment. Unfortunately,
59 phenotypic data are often obtained using laboratory-specific protocols, resulting in self-contained datasets
60 that are difficult to relate to one another for larger scale analyses. To enable meta-analyses of morphological
61 variation, particularly in the craniofacial complex and brain, we created MusMorph, a database of
62 standardized mouse morphology data spanning numerous genotypes and developmental stages, including
63 E10.5, E11.5, E14.5, E15.5, E18.5, and adulthood. To standardize data collection, we implemented an atlas-
64 based phenotyping pipeline that combines techniques from image registration, deep learning, and
65 morphometrics. Alongside stage-specific atlases, we provide aligned micro-computed tomography images,
66 dense anatomical landmarks, and segmentations (if available) for each specimen ($N=10,056$). Our workflow
67 is open-source to encourage transparency and reproducible data collection. The MusMorph data and scripts
68 are available on FaceBase (www.facebase.org, doi.org/10.25550/3-HXMC) and GitHub
69 (<https://github.com/jaydevine/MusMorph>).

70 **Keywords:** Mouse, phenomics, craniofacial, imaging pipelines, deep learning, morphometrics,
71 micro-computed tomography, FaceBase

72

73

74

75

76

77

78

79

80

81 **Background & Summary**

82 Understanding how genes, development, and the environment produce variation in complex morphological
83 traits is a core challenge in biology with evolutionary and clinical implications. Explanations for the
84 generation of variation tend to cohere around the genotype-phenotype map concept. Genetic variation and
85 genetic effects, like epistasis and pleiotropy, drive variation in developmental processes that act at different
86 times and scales in anatomical context¹⁻³. Specific developmental and genetic mechanisms then operate
87 alongside embedded mechanisms, such as nonlinearities^{4,5} and gene redundancy⁶, to modulate these effects
88 to express a phenotype⁷⁻⁹. Despite recent insights into these phenomena, the developmental-genetic basis
89 for morphological variation remains largely unknown, as there are likely many overlapping and coordinated
90 mechanisms involved, each with relative contributions¹⁰. To help disentangle these mechanisms, it is
91 important to build and integrate large phenotypic databases for model organisms¹¹⁻¹⁴. In this work, we
92 present MusMorph, a database of standardized mouse morphology data for meta-analyses of morphological
93 variability and variation, particularly in the craniofacial complex and brain.

94 The laboratory mouse is a useful model organism for studying the mechanisms of morphological
95 variation because of its 99% genetic homology with humans, short gestation, and rich set of tools for
96 manipulating the genome in a controlled environment. Unfortunately, phenotypic data are often biased by
97 laboratory-specific data collection protocols. The International Mouse Phenotyping Consortium (IMPC,
98 www.mousephenotype.org) was born out of a need to determine the relationship between genotype and
99 phenotype with standardized phenotypic data. Using micro-computed tomography (μ CT) and optical
100 projection tomography, the consortium has studied the anatomy of mouse lines heterozygous or
101 homozygous for a single gene mutation, particularly at embryonic day E9.5, E14.5-15.5, and E18.5¹⁵⁻²⁰.
102 Less emphasis has been placed on μ CT imaging and analysis of adults and mid-gestation (E10 to E11)
103 mutants, where critical developmental events, like fusion of the craniofacial prominences, occur. Mouse
104 lines with normal (non-pathological) levels of variation, such as recombinant inbred strains and outbred

105 strains with high heterozygosity²¹⁻²³, have also been poorly characterized. Quantifying such variation is
106 important, because it drives disease susceptibility and course of disease in humans.

107 Recently, model organism phenotyping has transitioned from manual linear measurements to fully
108 automated computational pipelines. One common approach is voxel-based morphometry^{24,25}. Voxel-based
109 morphometry is based on the analysis of deformation fields obtained via image registration. After spatially
110 aligning images to an average atlas, the deformation fields can be quantitatively compared between groups
111 on a voxel-wise basis to identify differences in morphology. Voxel-based morphometry remains a pillar of
112 shape analysis, because it can localize small regions of shape change without any *a priori* knowledge of the
113 anatomy, but it is prone to the multiple testing problem^{26,27}. Another approach is atlas-based geometric
114 morphometrics, which instead uses registration fields to automatically derive landmarks, or Cartesian
115 coordinate points that are homologous across samples. Geometric morphometrics is central to evolutionary
116 biology and developmental biology, among other fields, because landmarks allow for statistically tractable
117 quantifications of morphological variation, as well as intuitive visualizations²⁸. These advantages continue
118 to fuel development of novel geometric morphometric pipelines and extensions²⁹⁻³³. Yet large-scale
119 morphometric analyses remain rare due to the sparsity of standardized landmark data.

120 Here, we introduce MusMorph, a database of standardized mouse morphology data generated with
121 an open-source, atlas-based phenotyping pipeline that integrates techniques from image registration, deep
122 learning, and morphometrics. We compiled the database ($N=10,056$) using μ CT scans of mice from a
123 variety of strain/genotype combinations and developmental stages, including E10.5, E11.5, E14.5, E15.5,
124 E18.5, and adulthood. Most of MusMorph is composed of head morphology data, but there are also whole-
125 body embryo data for different integrative analyses. We provide (1) a developmental atlas for each
126 timepoint; (2) a rigidly aligned and preprocessed μ CT scan, dense anatomical landmarks, and
127 segmentations (if available) for each specimen; (3) a set of scripts for transforming and comparing an input
128 scan to an atlas; (4) an approach to validate the transformed landmark data and optimize it, if needed. To
129 ensure reproducibility and data sharing, we make the data freely accessible from FaceBase³⁴

130 (www.facebase.org, doi.org/10.25550/3-HXMC)³⁵ and our code from GitHub
131 (<https://github.com/jaydevine/MusMorph>). By incorporating substantial developmental and genetic
132 variation alongside a rich set of metadata, MusMorph will enable standardized morphometric analyses of
133 genotype-phenotypes to better understand the mechanistic basis for morphological variation.

134 Methods

135 Mice

136 We compiled mouse embryos and adults from numerous sources. The mouse lines for the E15.5 and E18.5
137 datasets were generated by the IMPC. These mice were produced and maintained on a C57BL/6N genetic
138 background, with support from C57BL/6NJ, C57BL/6NTac or C57BL/6NCrl. More details about
139 husbandry practices can be found at <https://www.mousephenotype.org/impress>. The mouse lines for the
140 E10.5, E11.5, E14.5, and adult datasets were produced on a variety of genetic backgrounds at different
141 institutions for studies of craniofacial variation. We hereafter refer to these lines as the Calgary mice,
142 because they were ultimately imaged at the University of Calgary. Specific information about study
143 protocols, such as husbandry practices and genotyping, should be gleaned from the MusMorph dataset
144 summaries on FaceBase or the original studies themselves. Each dataset within the MusMorph project on
145 FaceBase represents a study or set of studies defined by a common study design that yielded similar mouse
146 lines. Details about the experimental design were obtained from the original studies listed in the
147 “Publication(s)” section of each dataset. In addition, we provide a supplementary comma-separated values
148 (CSV) file (Study_Metadata.csv) in the project-wide metadata dataset³⁶ on FaceBase that lists the associated
149 studies.

150 Micro-computed tomography

151 **Sample preparation.** Each IMPC embryo underwent a hydrogel stabilization protocol³⁷ to prepare for
152 diffusible iodine-based contrast-enhanced μ CT (diceCT)³⁸. This involved incubating the embryo in a

153 hydrogel solution composed of 4% (wt) paraformaldehyde, 4% (wt/vol) acrylamide (Bio-Rad, USA),
154 0.05% (wt/vol) bis-acrylamide, 0.25% VA044 Initiator (Wako Chemicals, USA), 0.05% (wt/vol) saponin
155 (Sigma-Aldrich, Germany), and phosphate-buffered saline at 4°C for 3 days. Following incubation, the air
156 in the specimen tube was replaced with nitrogen gas and the tube was immersed in a 37°C water bath for 3
157 h. The whole embryo was then stained with a 0.025 N to 0.1 N Lugol's iodine (I₂KI) solution (Sigma-
158 Aldrich, Germany) for 24 h and mounted in agarose for diceCT. This approach has become a popular
159 alternative to magnetic resonance imaging because it is faster, cheaper, and still offers remarkable contrast,
160 allowing for high-throughput phenotyping of soft and hard tissue³⁸.

161 The Calgary embryos were subjected to different fixation and staining protocols. Each embryo
162 acquired prior to 2017 was fixed in a solution of 4% (wt) paraformaldehyde and 5% (wt) glutaraldehyde.
163 The specimen was next submerged in the CystoCon Ray II (iothalamate meglumine) contrast agent for one
164 hour to stain external morphology. Embryos obtained after 2017 were put through a nucleic acid
165 stabilization protocol that allows for examination of RNA in embryos scanned via μCT³⁹. Each embryo was
166 fixed with the PAXgene Tissue FIX solution (Qiagen, PreAnalytics, cat #765312), incubated overnight (17
167 h +/- 1 h) at room temperature, then transferred to a solution of PAXgene Tissue STABILIZER prepared
168 to manufacturer specification (Qiagen, PreAnalytics, cat #765512). For diceCT, each specimen was placed
169 in a solution of PAXgene Tissue STABILIZER and 1% to 3.75% (wt/vol) Lugol's iodine for 24 h. The
170 head of every embryo was dissected before being mounted in either agarose or soft wax, which was covered
171 by a microcentrifuge tube and infused with 50-100 μl of tissue stabilizer.

172 Each Calgary adult was set up with a standardized storage and mounting protocol. The mouse
173 carcass was stored at -20°C after euthanasia. Prior to the day of scanning, the mouse was retrieved and
174 thawed overnight at 4°C. The carcasses were then wrapped in foam and placed into a 37 mm diameter
175 sample holder for μCT.

176 **Imaging.** The IMPC embryos were imaged at six centers, including the Baylor College of Medicine, Czech
177 Center for Phenogenomics, MRC Harwell, Toronto Centre for Phenogenomics, The Jackson Laboratory,

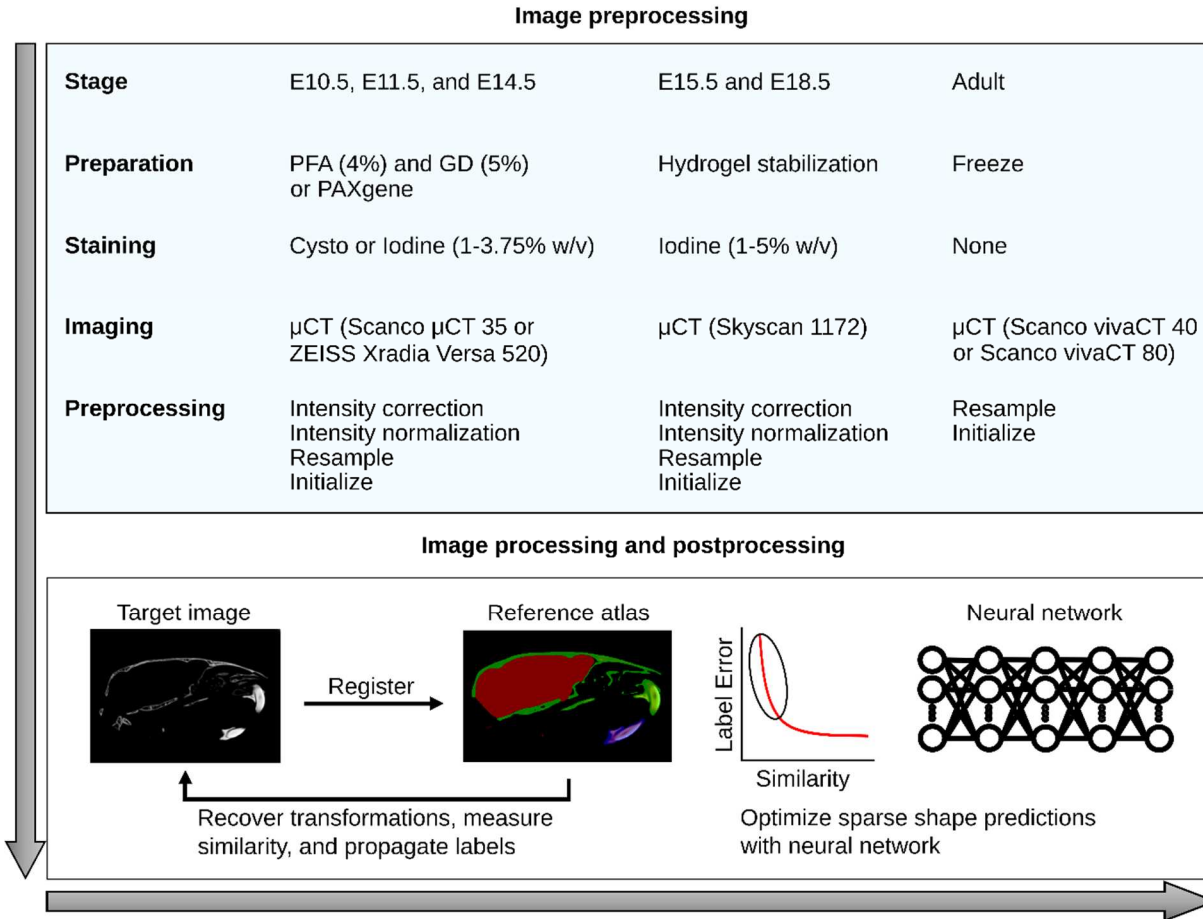
178 and University of California, Davis. A 3-D image of each iodine-stained whole embryo was acquired with
179 a Skyscan 1172 μ CT scanner (Bruker, Kontich, Belgium) at 100 kVp and 100 μ A. The raw images were
180 initially obtained with isotropic voxels but variable spatial dimensions and resolutions, ranging between
181 0.002 mm to 0.04 mm. Image projections were reconstructed into a digital stack using the Feldkamp
182 algorithm⁴⁰.

183 The Calgary mice were imaged in the 3-D Morphometrics Center at the University of Calgary. A
184 3-D image of each stained embryo head was obtained with either (a) a Scanco μ CT 35 scanner (Scanco
185 Medical, Brütsellen, Switzerland) at 45 kV and 177 μ A or (b) a ZEISS Xradia Versa 520 X-ray microscope
186 (Carl Zeiss AG, Oberkochen, Germany) at 40-50 kV, 4-5 W, and 2 s exposure time. A 3-D image of each
187 adult skull was acquired with either (a) a Scanco vivaCT 40 μ CT scanner (Scanco Medical, Brütsellen,
188 Switzerland), (b) a Scanco vivaCT 80 μ CT scanner (Scanco Medical, Brütsellen, Switzerland), or (c) a
189 Skyscan 1173 v1.6 μ CT scanner (Bruker, Kontich, Belgium) at 55-80 kV and 60-145 μ A. Like the IMPC
190 data, these original images were obtained with isotropic voxels but variable spatial dimensions and
191 resolutions. Embryo image resolutions ranged between 0.007 mm and 0.027 mm, whereas adult resolutions
192 ranged between 0.035 mm and 0.044 mm. Image projections were reconstructed with the integrated Scanco
193 software, the ZEISS XMReconstructor software, or the Skyscan NRecon v1.7.4.2 software.

194 **Image preprocessing**

195 We preprocessed each image to account for differences in image acquisition that would interfere with the
196 atlas-based registration workflow described below (Fig. 1). The preprocessing scripts are provided in the
197 MusMorph GitHub repository (<https://github.com/jaydevine/MusMorph/tree/main/Preprocessing>). In this
198 preprocessing step, we first converted the reconstructed imaging data (.nrrd, .aim, .tiff) to the Montreal
199 Neurological Institute (MNI) .mnc format using file conversion scripts written in Bash and Python (see
200 AIM_to_MNC.sh, NII_to_MNC.sh, TIFF_to_MNC.sh, DCM_to_MNC.sh, and NRRD_to_MNC.py). As
201 part of the open-source MINC library (<http://bic-mni.github.io/man-pages/>), the .mnc format is

202 implemented using HDF5 (Hierarchical Data Format, version 5), which supports hierarchical data structure,
203 internal compression, 64-bit file sizes, and other modern features⁴¹.



204 **Figure 1.** Schematic overview of the phenotyping pipeline. Specimens were staged, prepared (fixed/stored),
205 stained, and imaged with different but standardized lab-specific protocols. While the E10.5, E11.5, E14.5,
206 and adult specimens were obtained in Calgary, the E15.5 and E18.5 specimens were acquired from the
207 IMPC. To account for differences in image acquisition (e.g., intensity artifacts, image resolution and
208 dimensions, and position), each image was subjected to a series of preprocessing steps. Next, each
209 preprocessed image was non-linearly registered to a stage-specific reference atlas with a detailed set of
210 landmarks and segmentations. We recovered deformation fields, landmarks, and segmentations (if
211 available) for each specimen. To optimize the landmark predictions of poorly registered specimens, as
212 measured by cross-correlation similarity, a downstream neural network was used.

213 Staining artifacts, such as extreme intensity gradients and variable penetrance, can bias the image
214 registration process. To minimize intensity inhomogeneities, we applied the N3 method⁴². Since many of
215 the E15.5 images had background noise, where the stained scanning medium was indistinguishable from
216 the anatomy, we employed a thresholding script in Bash (see Threshold.sh). This script computes a lower

217 anatomical density threshold, masks the voxels above this bound and those in proximity via dilation, and
218 equates all voxels outside the mask to 0. To ensure the image resolutions and dimensions were consistent
219 with the atlas, we implemented an image resampling script in Bash (see Downsample_and_Correct.sh). We
220 also used this script to control for differences in bit depth among scanners by including a min-max
221 normalization, which scaled the embryo intensities between 0 and 1. Table 1 outlines the source of the
222 image data, developmental stage, voxel dimensions, image resolutions, stage-specific sample sizes, and the
223 presence or absence of atlas anatomical labels. Note that the E14.5 images were solely used to create another
224 stage-specific atlas, as they are from a smaller, unpublished dataset.

Table 1. Summary of imaging data. Source is where the image was acquired. Stage is the age of the specimen at sacrifice. Anatomy is the labelled and scanned anatomy. X, Y, and Z are the voxel lengths of each atlas axis. Resolution is the isotropic resolution of each scan. N is the sample size, with the number of scans awaiting publication of primary research in parentheses. Landmarks and segmentations indicate the presence (✓) or absence (✗) of labels on the stage-specific atlas.

Source	Stage	Anatomy	X	Y	Z	Resolution (mm)	N	Landmarks	Segmentations
Calgary	E10.5	Head	220	295	350	0.012	434	✓	✗
Calgary	E11.5	Head	502	503	390	0.012	531	✓	✗
Calgary	E14.5	Head; Body	486	567	723	0.027	84 (84)	✓	✗
IMPC	E15.5	Head; Body	486	567	723	0.027	1426	✓	✓
IMPC	E18.5	Head; Body	293	414	667	0.054	1657	✓	✗
Calgary	Adult	Skull	642	586	979	0.035	6000 (154)	✓	✓

225
226 Another essential step to all image registration workflows is the initialization, or a rigid alignment
227 between an image pair. Using initialization scripts written in Bash (see Preprocessing.md) and R
228 (Tag_Combine.R), we rigidly transformed each image to a stage-specific atlas or, if an atlas did not exist,
229 an arbitrary but stage-specific reference image. To determine the rigid transformation matrices, we utilized
230 a manual and automated approach, or a strictly automated approach, depending on anatomical orientation.
231 If the mouse was scanned in a random orientation, we rendered a minimum threshold surface in MINC,

232 then manually placed five homologous three-dimensional (3-D) landmarks at anatomical extrema (e.g.,
233 ears, nose, top of the head, and back of the head), resulting in an MNI tag point file (.tag) with landmark
234 coordinates. Next, we concatenated the reference and arbitrary landmark matrices, and minimized their 3-
235 D Euclidean distances via least squares. If the specimen was already roughly aligned to the reference image,
236 we performed an automated, intensity-based rigid alignment using the full registration process outlined
237 below (see the “Image Registration and Label Propagation” section). This intensity-based rigid alignment
238 was also repeated for the manually aligned volumes to ensure consistency. With the rigid transformation
239 matrices, we resampled each image into their stage-specific reference coordinate space using tri-linear
240 interpolation.

241 Reference atlases

242 We generated a population average atlas for each stage, excluding E15.5 and adulthood, by spatially
243 normalizing 25 μ CT images of wildtype mice with a group-wise registration workflow^{43,44} (Fig. 2 and 3).
244 A nearly identical workflow was used to create the existing E15.5 and adult atlases. The atlas construction
245 script is available in the MusMorph GitHub
246 (<https://github.com/jaydevine/MusMorph/tree/main/Processing>) and is written in Python (see
247 HiRes_Atlas.py or LoRes_Atlas.py). This script produces Bash scripts that can be executed automatically
248 and in parallel on a compute cluster to maximize computational efficiency. Without massively parallel
249 computing, the volumetric registrations would need to be performed sequentially, each requiring hours of
250 computation and a large amount of memory. Before executing the workflow, the user must upload the
251 initialized images and registration scripts to a compute cluster. In addition, the user needs to install a MINC
252 Toolkit module onto the cluster via Docker (<https://bic-mni.github.io/>) or GitHub (<https://github.com/BIC-MNI/minc-toolkit-v2>), or define a pre-existing module, because the scripts utilize the open-source MINC
253 software. An atlas can also be generated locally, but it will be significantly slower without massively
254 parallel computing.

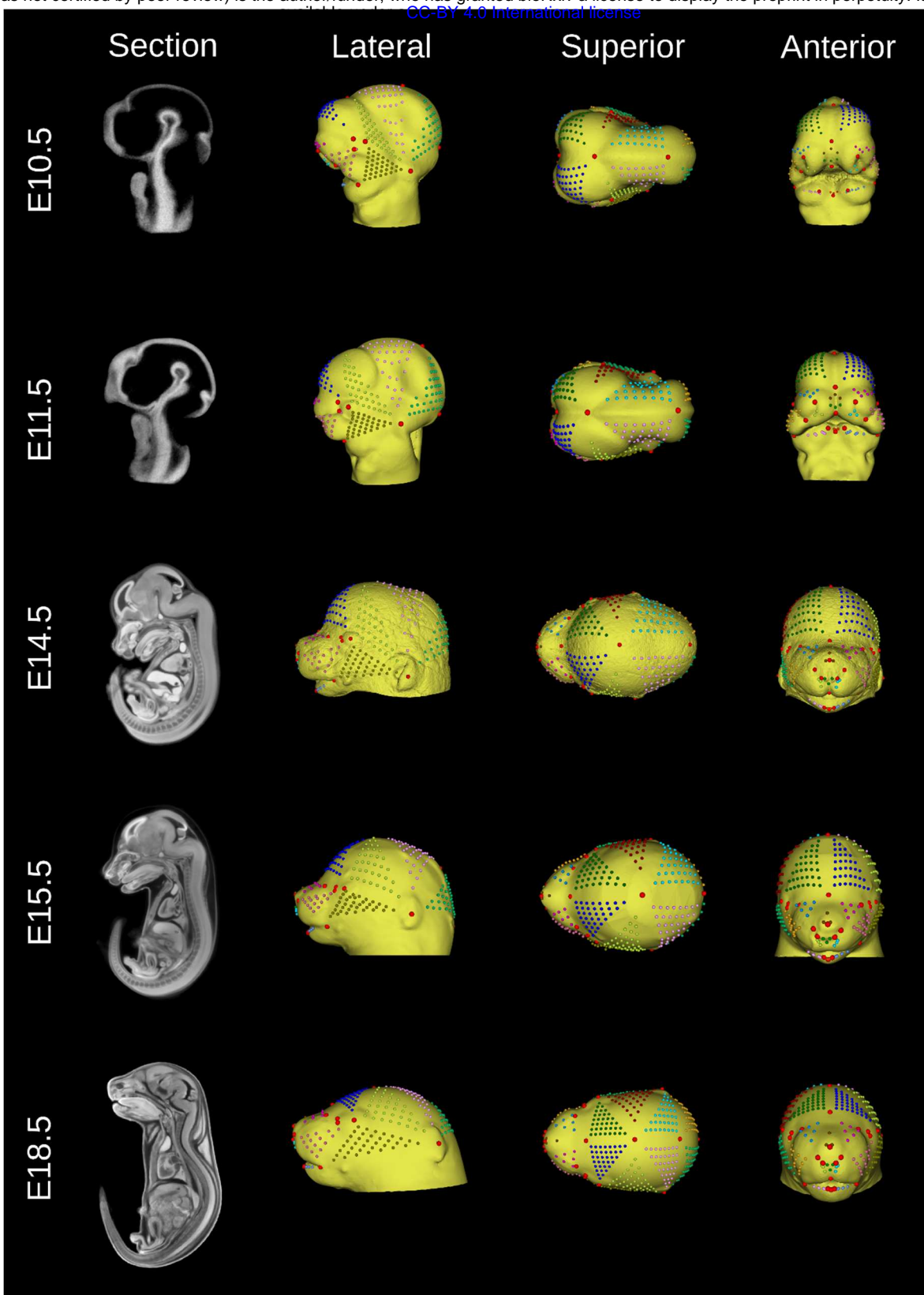
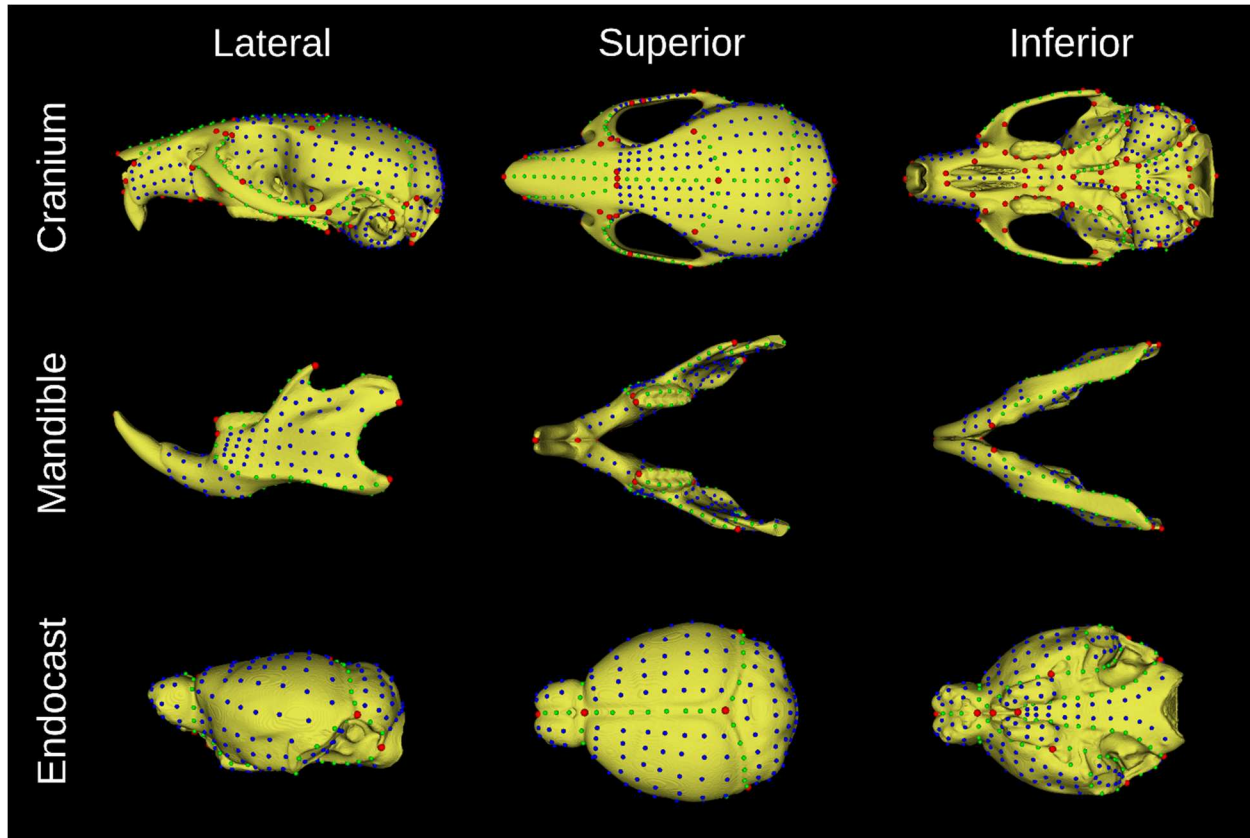


Figure 2. Embryo reference atlases. Sagittal cross-sections of the E10.5 (www.facebase.org/id/6-F00W), E11.5 (www.facebase.org/id/6-F012), E14.5 (www.facebase.org/id/6-F016), E15.5 (www.facebase.org/id/6-F6SE), and E18.5 (www.facebase.org/id/6-F6T4) atlas volumes are shown to display the stained internal anatomy. Each head surface was labelled with a dense landmark configuration to capture global and local aspects of morphology. Lateral, superior, and anterior views of each head isosurface are shown. The semi-landmark patches (small, color-coded points) were interpolated between a set of sparse homologous landmarks (large, red points). They can be slid and resampled for morphometric analyses.

257 Spatial normalization involves an initial affine transformation for global alignment, followed by a
258 deformable transformation for non-linear alignment. To account for global variation in location, orientation,
259 and scale, we computed a series of multi-resolution (coarse to fine) affine transformations among the
260 images by optimizing a cross-correlation objective function⁴⁵. Given that sample-wide pairwise
261 registrations yield an improved affine template⁴⁶, or intensity average, we completed all possible ($N=25*24$)
262 pairwise affine registrations, then averaged the resulting transformation for each specimen. Using the
263 averaged transformations, we resampled each initialized image into the affine coordinate space with tri-
264 linear interpolation and averaged the resulting images to produce an affine template. To correct for local
265 variation in shape, we computed a series of multi-resolution non-linear transformations with the ANIMAL
266 (Automatic Nonlinear Image Matching and Anatomical Labelling) algorithm⁴⁷, again optimizing for cross-
267 correlation. This iterative, four-step process involves non-linearly deforming each mouse to an evolving
268 template at increasingly higher resolutions, with the first template being the affine average and the next
269 three being improved versions of the non-linear average⁴⁸. The final product is a stage-specific average with
270 excellent contrast and a high signal-to-noise ratio.

271 Since the goal of MusMorph was to aggregate landmark data for morphometrics, and our primary
272 imaging data are head scans, we focused on labelling each atlas head surface with a standardized landmark
273 configuration (Fig. 2 and 3). Specific information about the number of landmarks and their anatomical
274 definitions can be found below in the “Data Records: Landmarks” section. To generate the landmarks, we
275 first rendered a minimum density isosurface in MINC, which uses ITK’s marching cubes algorithm, and
276 saved the 3-D rendering as a Stanford PLY (.ply) file. We then used 3D Slicer⁴⁹ or the MINC Toolkit to
277 acquire a landmark configuration on each surface that provided a comprehensive representation of shape⁵⁰.
278 For the embryos, we used 3D Slicer and the SlicerMorph extension³² to identify sparse landmarks and
279 interpolate landmark patches of variable density in between, depending on the size of the area, resulting in
280 dense coverage of the head. This also ensured that the patches were homologous, allowing for a
281 developmental morphospace into which all specimens may be superimposed. Because developmental

282 homology was not a consideration for the adults, we landmarked the adult atlas in MINC using built-in
283 display tools, again ensuring sparse and dense landmark coverage.



284 **Figure 3.** Adult reference atlas. Cranium (top), mandible (middle), and endocast (bottom) surfaces were
285 segmented from the skull atlas (www.facebase.org/id/6-F6VC), then labelled with a dense landmark
286 configuration to capture global and local aspects of morphology. Lateral, superior, and anterior views of
287 each segmentation isosurface are shown. There are sparse landmarks (red) as well as surface (blue) and
288 curve (green) semi-landmarks that can be slid and resampled for morphometric analyses.

289 Shared developmental pathways lead to correlated morphological variation, or morphological
290 integration⁵¹⁻⁵⁷. To enable analyses of integration, we added landmark configurations to segmented surfaces
291 of the adult skull atlas. We manually segmented the cranium, mandible, and neurocranial endocast (i.e., a
292 proxy for the brain) in MINC, then rendered these segmentations as isosurfaces before landmarking them
293 with a dense configuration. Once again, the landmark details are described below in the “Data Records:
294 Landmarks” section. The segmentations may further be used for surface-based analyses⁵⁸, measures of size
295 (e.g., volume or surface), or as masks to reduce the shape dimensionality of a voxel-based morphometry
296 analysis. Unlike the adult atlas, the embryo atlases do not come with segmentations due to the scope of this

297 work, apart from the pre-existing E15.5 atlas, which has 48 manually segmented structures
298 (http://www.mouseimaging.ca/technologies/mouse_atlas/mouse_embryo_atlas.html).

299 Image registration and label propagation

300 We pairwise registered each image to their stage-specific atlas to obtain a composite (affine and non-linear)
301 transformation for label propagation (Fig. 1). Like the atlas workflow described above, the registration
302 scripts are available in the MusMorph GitHub
303 (<https://github.com/jaydevine/MusMorph/tree/main/Processing>) and are written in Python (see
304 HiRes_Pairwise.py or LoRes_Pairwise.py). The purpose once more is to produce Bash scripts *en masse* for
305 massively parallel computing on a compute cluster due to the computational requirements of volumetric
306 deformable registration and anatomical labelling. Only the initialized images and registration scripts need
307 to be uploaded to the cluster to execute the workflow. While the pairwise registrations involved the same
308 multi-resolution affine alignment described above, the non-linear alignment differed. Here, we
309 implemented the geodesic SyN (Symmetric Normalization) algorithm⁵⁹, because it was previously
310 validated for atlas-based landmarking and morphometrics of mouse models⁴⁴. The SyN registrations were
311 optimized using cross-correlation. After registration, we used labelling scripts written in Bash and produced
312 via Python (see Label_Propagation.py) to recover the non-linear transformations, concatenate them with
313 the affine transformations, invert them, and propagate the atlas labels to the rigid space of each image.

314 Neural network shape optimization

315 Although top-performing registration algorithms provide an effective and generalizable way to
316 automatically label anatomy, there are instances where outliers and problematic landmarks can alter shape
317 representations. This is particularly true for model organisms, where mutant phenotypes may show little to
318 no resemblance with an atlas. To demonstrate how biological signal can be restored, we implemented a
319 supervised deep learning workflow available in the MusMorph GitHub
320 (<https://github.com/jaydevine/MusMorph/tree/main/Postprocessing>), which employs scripts written in R

321 and Julia (see GPA_and_Projection.R and Landmark_Optimization.jl)⁶⁰. Using a subset of 68 sparse adult
322 craniofacial landmarks ($N=2,000$) described in previous work⁶¹⁻⁶⁵, we trained a deep feedforward neural
323 network to learn a domain-specific loss function that minimizes automated and manual shape differences.
324 The sparse landmark numbers amenable to optimization (see Optimization_Order.csv)³⁶ are available on
325 FaceBase. We focused on the adults because that was the only stage with a large existing set of homologous
326 manual landmarks for training.

327 We tested the network predictions on a random subset ($N=500$) of adult skulls described further in
328 the “Technical Validation” section. To help others initialize the network without having to retrain it, we
329 provide the adult network model (Calgary_Adult_Cranium_Model.bson) and weights
330 (Calgary_Adult_Cranium_Weights.bson) in the Binary JSON (.bson) file format on GitHub. We also make
331 available the optimized sparse shape predictions for the entire adult crania dataset
332 (Adult_Cranium_Sparse_Landmarks.csv)³⁶. Although we focused on adults, this optimization strategy is
333 generalizable, so other research groups with manual landmark data on any structure of the atlases may use
334 the network architecture to improve outlier predictions.

335 **Data Records**

336 Specimen metadata

337 Each specimen is associated with a rich set of identifiers to accommodate morphometric analyses using
338 multiple factors and/or covariates. Alongside detailed metadata descriptions in FaceBase, we provide the
339 specimen metadata as a supplementary CSV file (MusMorph_Metadata.csv)³⁶ for convenience and to
340 include auxiliary fields. Table 2 enumerates the metadata and Table S1 summarizes the metadata
341 distributions for each dataset on FaceBase.

Table 2. Summary of metadata identifiers.

Identifier	Description
Biosample	The name of the specimen, which corresponds to the image and label names.
Strain	The background strain of the specimen.
Strain_MGI_ID	The MGI ID for the strain.
Strain_Type	An attribute of strain that describes whether it is inbred or outbred and lab-derived or wild-derived.
Gene	The gene symbol as provided by MGI.
Gene_MGI_ID	The MGI ID for the gene.
Zygosity	Whether the specimen is homozygous, heterozygous, wildtype, or otherwise (e.g., flox/null) for a given gene mutation.
Genotype	A concatenation of the gene symbol and zygosity symbol.
Anatomy	The region of anatomy that has been scanned and labelled.
Treatment	An environmental effect that the specimen has been treated with.
Experimental Group	An identifier derived from genotype that denotes whether the specimen is a control or mutant.
Sex	The sex of the specimen.
Stage	The age of the specimen in days, either embryonic (E) or postnatal (PN).
Life_Phase	An identifier derived from stage that indicates life phase (e.g., gestation vs. adulthood).
Dataset	The published or unpublished study (see Study_Metadata.csv) the sample is associated with.
Availability	Whether the images and phenotypic data are available or pending publication of a primary research article.

342

343 Fig. 4a-b illustrates the distributions of sex, strain type, and genotype across the embryo and adult
344 datasets. Sex is well-annotated for the E15.5, E18.5, and adult datasets, but is missing (“NA”) for many of
345 the E10.5 and E11.5 specimens. While most of the embryo mouse models were produced on an isogenic
346 inbred background, particularly C57BL/6N, strain diversity is a focal point of the adult datasets. Among
347 the nine adult strain types provided, there are 98 unique background strains. The majority are recombinant
348 inbred lines (e.g., the Collaborative Cross dataset⁶⁶), wild-derived crosses (e.g., the Hybrid dataset⁶⁷), and
349 outbred lines (e.g., the Diversity Outbred dataset⁶⁸). We have included 459 unique genotypes for the embryo
350 datasets, most of which derive from the IMPC dataset⁶⁹, as well as 179 genotypes for the adult datasets. A
351 minority of specimens, including several embryos in the Ap2⁷⁰, B9d⁷¹, and Bulgy⁷² datasets as well as a
352 few adults in the Brain-Face⁷³ dataset, have unknown genotypes (e.g., “-/-;NA” and “+/-;NA” in double

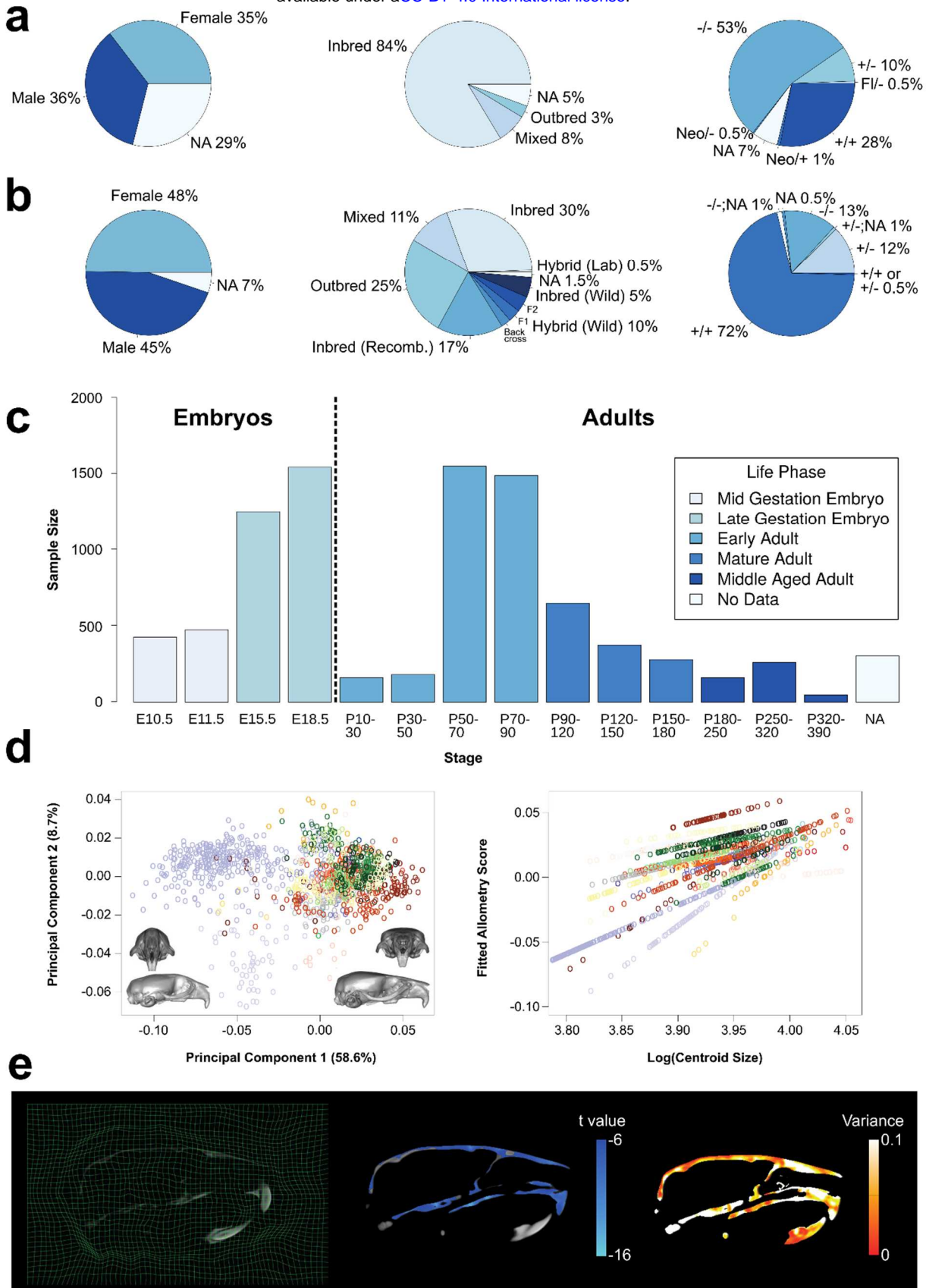


Figure 4. Summary of metadata. (a) Distribution of sex, strain type, and genotype for the embryo datasets. (b) Distribution of sex, strain type, and genotype for the adult dataset. (c) Sample sizes of each developmental stage included in the database. All “NA” specimens are mature or middle-aged adults. (d) Left: Example landmarks and segmentations of the adult skull and endocast (brain). Middle/Right: Morphological analyses, such as PCA and allometry regressions, that one might perform with a dense landmark dataset. Each color in the plot represents a different mouse genotype.

(e) Left: Slice visualization of a non-linear deformation grid. Middle/Right: Morphological analyses, such as statistical parametric mapping, that one might perform with a deformation field. The *t* values show significant ($p < 0.05$) voxel-wise differences in form (i.e., volume shrinkage) in *Ghrhr* homozygous mutants relative to wild type, whereas the variance heatmap shows voxel-wise variances in *Ghrhr* mutants.

354 knockout designs or “NA” and “+/+ or +/-” in single knockouts) due to genotyping complications in the
355 past. Specimens homozygous for a single gene mutation predominate the embryo datasets, whereas normal
356 wildtype variants comprise the bulk of the adult datasets. Fig. 4c shows the developmental stages
357 represented in MusMorph. Of the 10,056 specimens processed, 40% are embryos and 60% are adults, many
358 of which have just finished maturing around postnatal day 90. All specimens without a recorded stage
359 (“NA”) are mature adults.

360 It is often desirable to compare mutants to their wildtype counterparts from the same sample
361 because background strains vary. To preserve sample provenance where possible, specimens that are
362 wildtype for a given mutation will have the same gene symbol as their heterozygote and homozygote
363 littermates. For wildtype specimens without litter information, like the IMPC dataset, their genotypes are
364 equated to background strain. Mouse strain nomenclature follows the MGI guidelines, except when the
365 strain design is unknown and has no MGI ID (e.g., novel hybrid backcrosses). We also abbreviate genotypes
366 for complex strain designs using MGI synonyms if available. Furthermore, while most wildtype specimens
367 fall within the control experimental group, there are cases where they can exhibit mutant-like phenotypes
368 and be categorized as such. One example in MusMorph is the artificial selection Longshanks dataset⁷⁴,
369 which through many generations of artificial selection produced wildtype specimens with extreme tibia and
370 craniofacial phenotypes^{75,76}.

371 We selected the above identifiers, because they tend to explain a significant amount of
372 morphological variation in morphometric analyses. For instance, many structures in the mouse are sexually
373 dimorphic, including the shape of the brain⁷⁷ and craniofacial complex⁷⁸, cortical bone size and strength⁷⁹,
374 adipose tissue distribution⁸⁰, and feto-placental growth^{81,82}, to name a few. It is also known that classical
375 laboratory strains, such as those in the Strain Comparison dataset⁸³, exhibit naturally occurring craniofacial

376 phenotypes⁸⁴. Moreover, gene mutations can interact with a background strain via epistasis to produce
377 different phenotypes⁸⁵⁻⁸⁷, like those in the Spry dataset⁸⁸. Another key driver of variation is developmental
378 stage, as differences in age often define a principal axis of allometric variation via correlations with size
379 and/or shape⁸⁹⁻⁹³. Given the ubiquity of allometry, these correlations can be found across most MusMorph
380 datasets (Fig. 4d). Finally, numerous studies have reported the phenotypic outcomes of single gene
381 mutations, environmental perturbations, and how zygosity modulates these effects⁹⁴⁻⁹⁶. These identifiers
382 have corresponding images, landmarks, segmentations, and deformation fields for morphological analyses
383 (Fig. 4d-e).

384 Images

385 We provide the atlases and initialized images for each specimen in the MNI .mnc format. The naming
386 convention for the atlas volumes is <Source>_<Stage>_<Anatomy>_Atlas.mnc. They are categorized as
387 “Imaging Data” in the project-wide dataset³⁶ on FaceBase. The naming convention for the initialized
388 volumes is <Biosample>.mnc, where *Biosample* is the name of the specimen in the metadata (see the
389 “Specimen metadata” section). One exception is the naming convention for the subset of thresholded E15.5
390 images, which is <Biosample>_Thresh.mnc. These volumes are also categorized as “Imaging Data” across
391 the MusMorph datasets on FaceBase. Each .mnc file has four key attributes: 1) a *named dimension* (*xspace*,
392 *yspace*, *zspace*), 2) *length* (number of voxels on each dimension), *step* (resolution), and *start* (origin). MINC
393 defines a voxel and world coordinate system, so one can move between them with the simple
394 “voxeltoworld” and “worldtovoxel” MINC commands. If users want to convert between .mnc and different
395 file formats (e.g., raw data, DICOM, NIfTI, Analyze, ECAT, TIFF, Concorde, VFF), there are a variety of
396 other Bash commands available (<http://bic-mni.github.io/man-pages/>). While the raw IMPC images are
397 freely accessible in the NRRD (.nrrd) format at <https://www.mousephenotype.org/data/embryo>, the raw
398 Calgary images are available upon request in the AIM (.aim) or TIFF (.tiff) formats.

399 Transformations

400 For each pairwise registration, we recovered an inverted non-linear and composite (affine and non-linear)
401 transformation. Given the file sizes of the non-linear deformation fields (~3 GB on average \times 10,000 = 30
402 TB), we make the transformations available upon request. The deformation fields and composite
403 transformations are in the MNI .mnc and .xfm formats. Each .mnc file shares the same image attributes
404 described above with an additional *named dimension* called *vector_dimension* which describes the non-
405 linear displacement vectors. Each .xfm file contains a header and affine transformation matrix. The naming
406 convention for the deformation fields is *<Biosample>_ANTS_nl_inverse_grid_0.mnc* and
407 *<Biosample>_ANTS_nl_inverse.xfm*, whereas the composite transformations are called
408 *<Biosample>_origtoANTSnl_grid_0.mnc* and *<Biosample>_origtoANTSnl.xfm*. “ANTS” denotes the
409 algorithm and “nl” stands for “non-linear”. Much like the images, the transformations for the subset of
410 thresholded E15.5 volumes have “Thresh” appended to the *<Biosample>* name.

411 Non-linear deformation fields describe the displacements of each target image voxel to each
412 reference image voxel⁹⁷. By calculating the Jacobian determinant J for every point $p(x, y, z)$ in the
413 deformation field,

$$414 \quad \det(J(x, y, z)) = \begin{vmatrix} \frac{\partial x}{\partial x} & \frac{\partial y}{\partial x} & \frac{\partial z}{\partial x} \\ \frac{\partial x}{\partial y} & \frac{\partial y}{\partial y} & \frac{\partial z}{\partial y} \\ \frac{\partial x}{\partial z} & \frac{\partial y}{\partial z} & \frac{\partial z}{\partial z} \end{vmatrix}$$

415 one can quantify the magnitude of morphological change at each voxel (Fig. 4e). A Jacobian determinant
416 of 1 indicates no volume change, whereas determinants greater than 1 indicate volume expansion and
417 determinants between 0 and 1 indicate volume shrinkage. These determinants can also be scaled and
418 sheared with a composite transformation to examine voxel-wise differences in form. Jacobian determinants
419 can be analyzed with voxel-wise tests, such as an ANOVA with a false-discovery rate correction, to map
420 statistics onto the anatomy, a technique otherwise known as statistical parametric mapping (see

421 VBM_Example.R). For example, in Fig. 4e, we use the *RMINC* R package (<https://github.com/Mouse->
422 Imaging-Centre/RMINC) to show significant voxel-wise changes (shrinkages) in form between *Ghrhr*
423 mutants⁹⁸ and wildtype specimens, as well as voxel-wise variances in form associated with this mutation.

424 Landmarks

425 We labelled each atlas, and thus every registered mouse embryo and adult, with a standardized landmark
426 configuration (Fig. 2 and 3). The atlas landmark files are named
427 <Source>_<Stage>_<Anatomy>_Atlas_Landmarks.tag. They are stored as “Imaging Data” alongside the
428 atlas volumes on FaceBase³⁶. The individual specimen landmark files are named
429 <Biosample>_<Anatomy>_Landmarks.tag and are similarly categorized as “Imaging Data” across
430 FaceBase. The MNI .tag file format is an ASCII file which stores the coordinates of each landmark in the
431 millimetric world space of the volume. Each .tag file has a header above an array of p landmarks (rows) in
432 k dimensions (columns). These files can be imported into R individually or collectively as a 3-D array using
433 the *tag2array* function in the custom *morpho.tools.GM* package⁹⁹. Alternatively, the user can employ the
434 *read.csv* function in R to import a vectorized .csv file. We provide landmark .csv files for every
435 developmental stage and anatomical region³⁶, each of which contains a matrix of n specimens (rows) and
436 $p \times k$ landmark coordinate dimensions (columns). Importantly, there are dense semi-landmarks and sparse
437 fixed landmarks for local and global geometric morphometric analyses of craniofacial, endocast (brain),
438 and mandible morphology. In Fig. 4d, for instance, we show craniofacial shape morphs along the first
439 principal component (PC) in an adult subsample, as well as allometry regressions which relate craniofacial
440 shape to size.

441 The embryo landmarks are homologous across stages. Table S2 describes the sparse embryo
442 landmarks and their biological definitions. Table S3 lists the embryo semi-landmark patches and their
443 density, both of which are based on the sparse landmarks. The stage-specific semi-landmark patch files can
444 also be found as tab-separated value (TSV) files on GitHub

445 (https://github.com/jaydevine/MusMorph/tree/main/Postprocessing). Each embryo has 22 sparse
446 homologous landmarks within their larger dense configuration. To perform a sparse landmark shape
447 analysis, users may subset the first 22 rows of each 3-D array. Since there are three additional sparse
448 landmarks for the E15.5 and E18.5 specimens, rows 23 to 25 may be included for stage-specific analyses
449 or excluded for ontogenetic analyses.

450 The adult landmarks are simply homologous within stage. Tables S4, S5, and S6 describe the sparse
451 adult craniofacial, endocast, and mandible landmarks, respectively, as well as their biological definitions.
452 While the adult curve semi-landmarks and surface semi-landmarks are not patch based, they can be slid and
453 resampled using the R scripts on GitHub (see `Calgary_Adult_Cranium_Sliding_Semis.R`,
454 `Calgary_Adult_Mandible_Sliding_Semis.R`, and `Calgary_Adult_Endocast_Sliding_Semis.R`) to mimic
455 patches or any other structure. Much like the embryos, the sparse landmarks are the first 93, 12, and 19
456 rows of the cranium, endocast, and mandible 3-D arrays, respectively, and can be partitioned for a sparse
457 shape analysis. If users want to generate new landmarks, such as internal landmarks or whole-body
458 landmarks, they can use a script (see `Label_Propagation.py`), the inverted composite transformations (see
459 the “Transformations” section), and a local or remote compute cluster to propagate the landmarks to an
460 initialized image. To promote standardization, we encourage users to add new landmark subsets to the pre-
461 existing configurations.

462 Segmentations

463 We provide segmentation labels for the E15.5 and adult atlases and specimens to support alternative
464 morphological analyses, such as 3-D visualizations, voxel-based morphometry, volumetric size
465 comparisons, and surface-based image processing pipelines. Other stages do not have segmentation labels
466 due to the scope of this work. The segmentations follow the same naming conventions described above:
467 `<Source>_<Stage>_Atlas_Segs.mnc` and `<Biosample>_Segs.mnc`. The atlas segmentations are available
468 as “Imaging Data” on FaceBase³⁶, as are the individual segmentation files across various MusMorph

469 datasets. The published E15.5 atlas contains 48 whole body segmentations
470 (http://www.mouseimaging.ca/technologies/mouse_atlas/mouse_embryo_atlas.html)⁴⁸, while the adult
471 atlas comes with cranium, endocast, and mandible segmentations. Each label file is a .mnc volume of
472 integers that matches the dimensionality of the image. To visualize the adult segmentations, for example,
473 the user may load the atlas and label files together and input an integer of 1 to render the endocast, 2 for the
474 cranium, and 3 for the mandible. As with new landmarks, there is the potential to resample new atlas
475 segmentation labels into the initialized space of any image using the composite transformations (see the
476 “Transformations” section) and a local or remote compute cluster (see `Label_Propagation.py`).

477 **Technical Validation**

478 *Cross-correlation and root mean squared error*

479 We computed intensity-based, pairwise registrations between each target image (I) and a reference atlas
480 (J) by optimizing a normalized cross-correlation (NCC) similarity metric:

$$481 NCC(I, J) = \frac{\sum_{p \in \Omega} I(p)J(p)}{\sqrt{\sum_{p \in \Omega} I(p)^2 \sum_{p \in \Omega} J(p)^2}}.$$

482 Normalized cross-correlation is calculated for all voxel positions p over a discrete domain ($p \in \Omega$). If the
483 domain is the entire 3-D volume and $NCC(I, J) = 1$, the deformed target image and reference image are
484 perfectly aligned. To assess the quality of each registration, we recorded the normalized cross-correlation
485 between each deformed target image and the atlas using code in the labelling scripts (see
486 `Label_Propagation.py`). Unfortunately, it is difficult to know whether the final registration correlations are
487 “good” or “bad” without relating them to the quality of the labels collected. We investigated the relationship
488 between landmark root mean squared error and cross-correlation in the adult crania training set above to
489 build a quality assessment model. Letting $x_\ell^{(I)}$ and $\widehat{x}_\ell^{(I)}$ denote the observed (manual) and predicted

490 (automated) Euclidean vectors at landmark ℓ for a target image I , the root mean squared error for p
491 landmarks is defined as

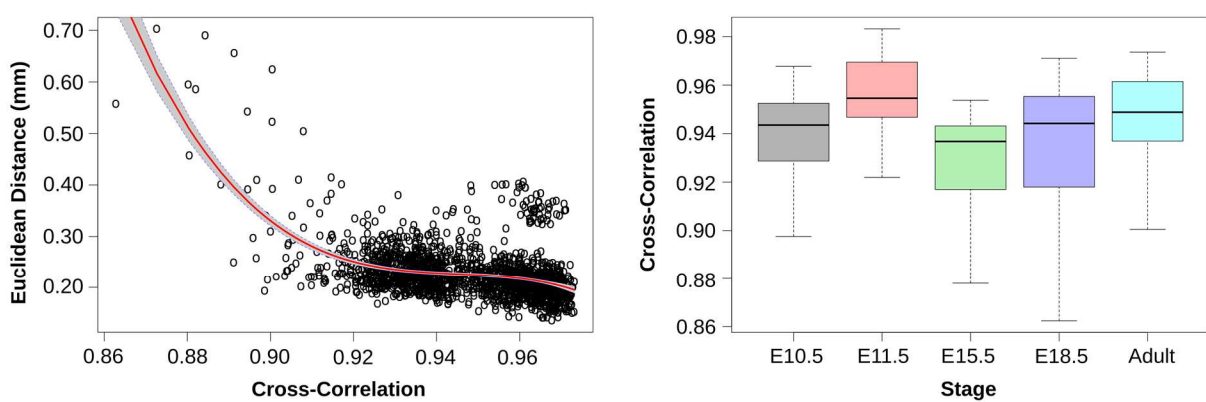
492
$$RMSE = \sqrt{\sum_{\ell=1}^p \frac{1}{n} \sum_{I=1}^n \left(\mathbf{x}_{\ell}^{(I)} - \widehat{\mathbf{x}}_{\ell}^{(I)} \right)^2}.$$

493 After computing the root mean squared error for each specimen, we regressed these values on their
494 corresponding cross-correlation values with linear, squared, and cubic cross-correlation terms (Fig. 5a). We
495 found a statistically significant non-linear relationship ($R^2 = 0.3$, $p < 0.001$), such that cross-correlation
496 values below 0.90 resulted in exponentially higher landmark errors. The average root mean squared error
497 was 0.23 mm (95% CI ± 0.002 mm). This mean error is comparable to manual landmark intra-observer
498 detection errors across the skull, which tend to be 0.25 mm or less^{44,50}. To verify registration quality across
499 the rest of the database, we calculated cross-correlations for all specimens and stages. The mean cross-
500 correlation values and their standard deviations for E10.5, E11.5, E15.5, E18.5, and adulthood were $0.94 \pm$
501 0.07 , 0.96 ± 0.04 , 0.93 ± 0.02 , 0.93 ± 0.12 , and 0.95 ± 0.02 , respectively (Fig. 5a). These values are on par
502 or higher than those reported in previous mouse registration studies¹⁰⁰ and speak to the reproducibility of
503 this approach for analyzing variable morphology.

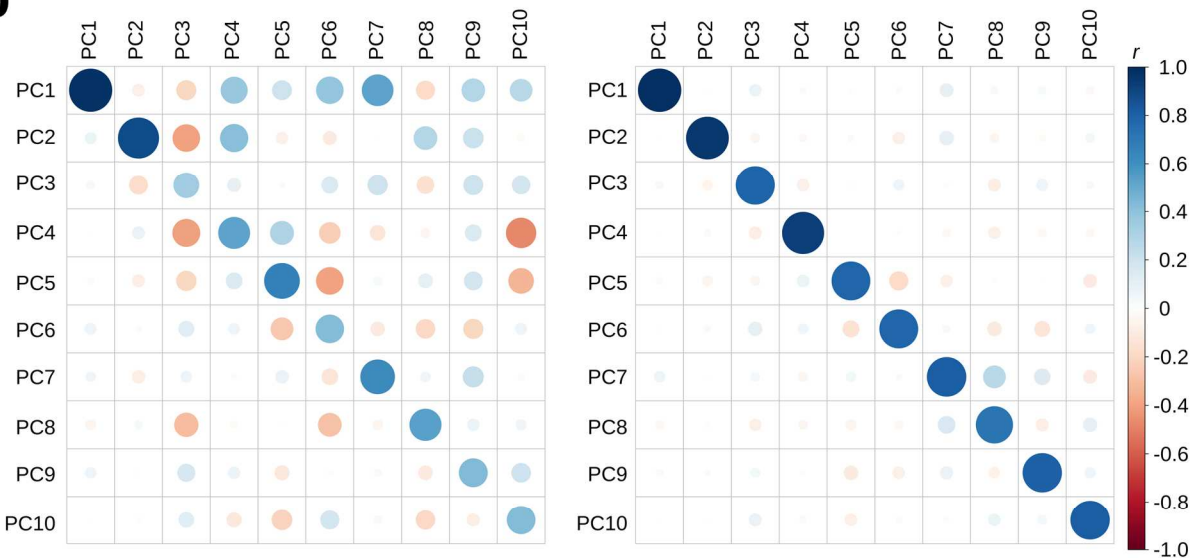
504 *Covariance patterns and the mean shape*

505 We quantified differences in covariance structure and the sample mean shape between our baseline
506 automated landmarks, the optimized neural network landmarks, and the manual landmarks. To analyze
507 covariance similarity, we projected the automated configurations into the manual PC space and correlated
508 the uncentered PC scores. Fig. 5b shows automated and manual correlations for the first 10 PCs (65.1% of
509 the total variance). The average correlation within PCs for the baseline automated configurations was $r =$
510 0.6. This measure is biased downwards by lower order automated PCs, which tend to capture residual
511 covariance of the first manual PC. The average correlation within PCs for the optimized automated
512 configurations was $r = 0.8$, suggesting a restoration of signal among the major PCs.

a



b



c

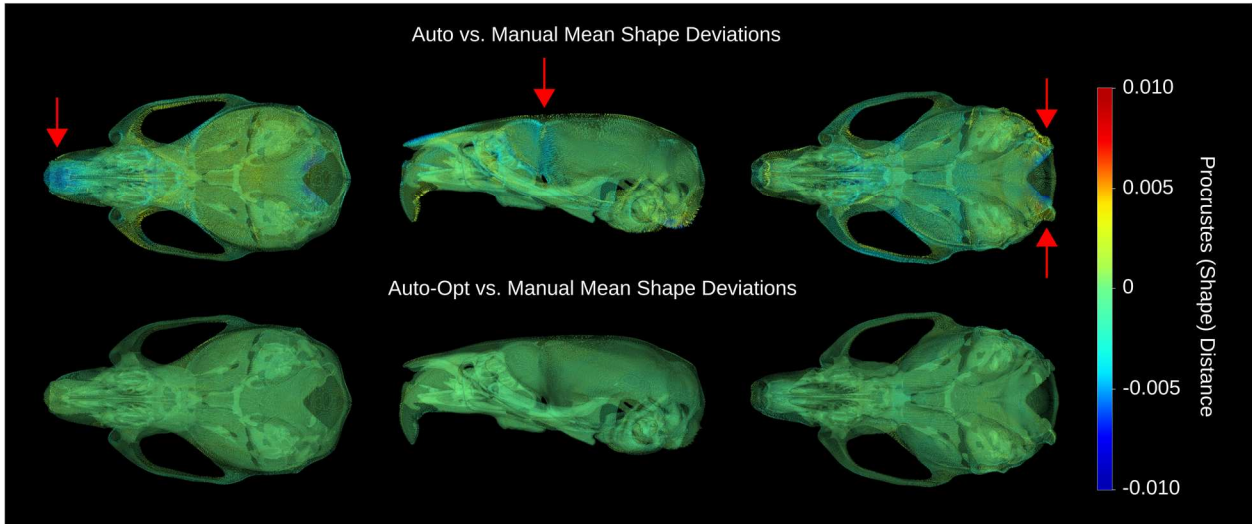


Figure 5. Validation of adult crania test set. (a) Left: Regression of automated-manual Euclidean distances (error) on cross-correlation, a measure of the final target-reference image similarity. Right: Boxplots showing the distribution of cross-correlation values within each developmental stage. (b) Correlation of automated and manual PC scores. Left: Baseline automated PC correlations. Right: Optimized automated PC correlations. (c) Mean shape deviations between the automated and manual datasets. Red arrows indicate error prone areas.

514 To analyze mean shape deviations, we computed the grand mean shape for the manual landmarks
515 and deformed it to the automated mean shapes via thin-plate spline. We then used the *Morpho* package¹⁰¹
516 in R to generate a deformation heatmap of Procrustes distances at every vertex of the deformed mesh (Fig.
517 5c). Procrustes distance is equivalent to the root mean squared error between two configurations in shape
518 space. The total distance between the baseline automated mean and manual mean was 0.05, whereas the
519 distance between the optimized automated mean and manual mean was 0.01. Visually, the baseline
520 automated mean shape is largely indistinguishable from the manual mean shape, apart from several known
521 problematic areas⁴². First, the anterior extent of the frontonasal prominence is underestimated. Second, the
522 shape of the foramen magnum is altered. Third, the lateral extent of the frontal bone is underestimated,
523 likely because there are no sparse landmarks to interpolate there; however, this area is well-covered by the
524 dense landmark configurations. Optimization successfully corrected errors at these problematic locations.

525 *Outliers and stage-specific shape distributions*

526 For each stage, we calculated the Procrustes distance between the mean shape and every configuration to
527 obtain shape distributions and identify outliers (Fig. S1). We defined outlier shapes as those with a
528 Procrustes distance above $Q_3 + 1.5 \times IQR$, where Q_3 is the third quartile and IQR is the interquartile range.
529 Next, we displayed a minimum threshold isosurface of each outlier image alongside its landmarks to assess
530 the errors. Landmark (.tag) files with clear head registration errors were removed. We observed most errant
531 outlier landmark configurations in the E15.5 and E18.5 embryos, which underwent whole-body
532 registrations. Since the orientation of the head relative to the body cannot be standardized in embryos, the
533 whole-body registrations and inherent constraints of spatial normalization resulted in local registrations
534 errors if their orientation was markedly different from the atlas.

535 Eliminating problematic outliers with distance distributions is a global solution but not always a
536 local one. For example, if a landmark configuration hardly deviates from the mean on average, yet still has
537 several landmarks with high detection errors, its distance to the mean could be small but its shape distinct.

538 We performed a Principal Component Analysis on each stage-specific landmark dataset (Fig. S2 and S3)
539 to identify such localized errors, assuming the first PC would capture distinctly problematic shapes. Fig. 6
540 shows the resulting shape distributions along PC1 for each stage. Here, we morphed a surface of the mean

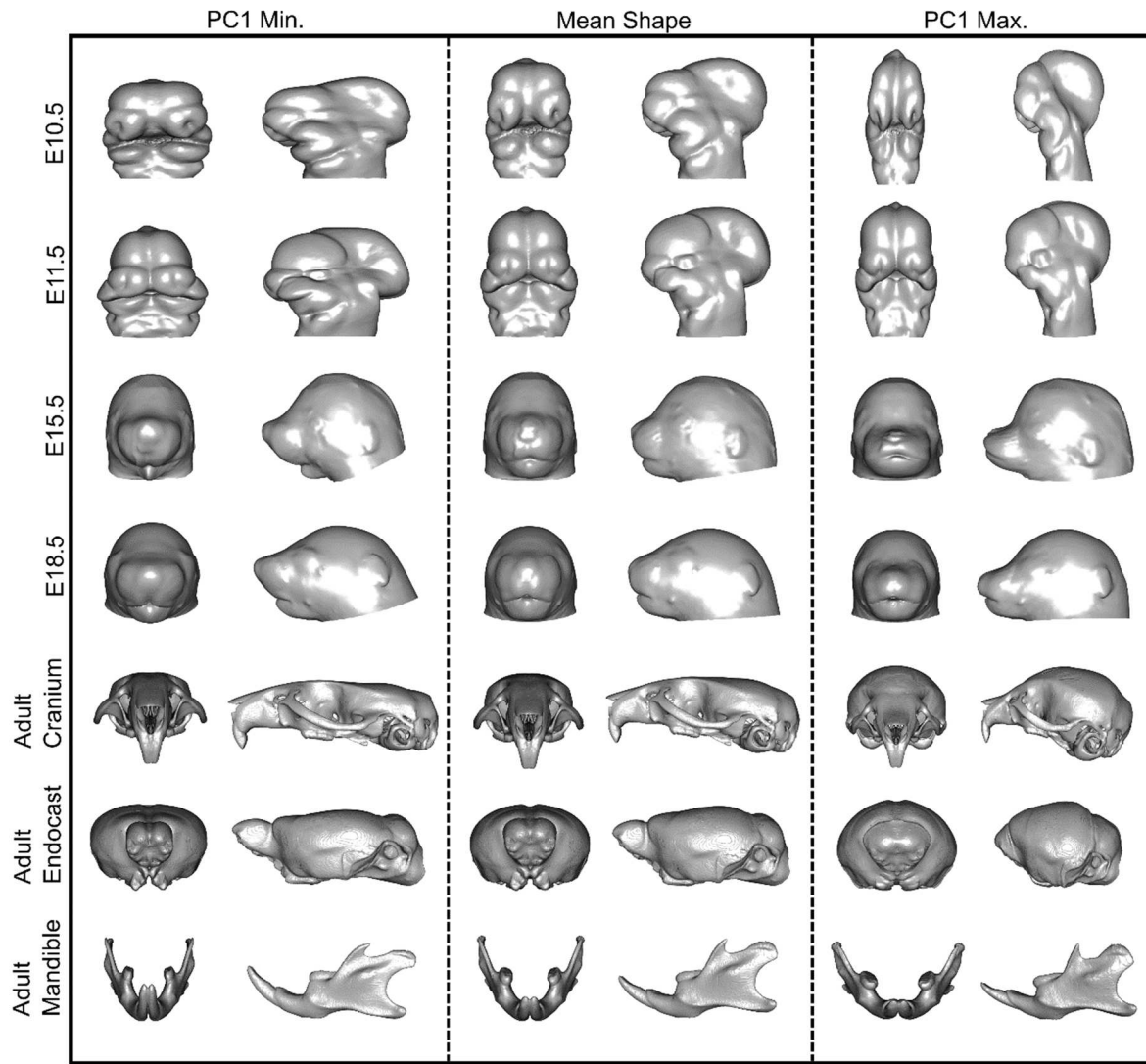


Figure 6. Principal Component Analysis of stage-specific shape data. The mean shape (center) was deformed to the minimum (left) and maximum (right) extremes of PC1. Every morph is shown with anterior and lateral views. Each row represents a different developmental stage, ranging from E10.5 to adulthood.

541 shape to each extreme via thin-plate spline and visualized the outputs. If the deformed surface was unusual,
542 we displayed the image and landmarks as above, removed the errant landmark (.tag) file if necessary, and
543 repeated this process until the prediction was correct.

544 **Discussion**

545 *Why MusMorph?*

546 The goal of MusMorph was to create a database of standardized mouse morphology data using an
547 automated, high-throughput, and open-source phenotyping pipeline. By combining developmental atlases
548 with a registration and deep learning framework, we constructed common coordinate systems into which
549 various phenotypic data can be integrated. We primarily focused on acquiring morphological data,
550 including anatomical landmarks, segmentations, and deformation fields, for the craniofacial complex and
551 brain. However, we also generated whole body data for other integrative analyses of late-gestation embryos.
552 To enable novel morphometric analyses of genotype-phenotype maps, we utilized mouse models with
553 substantial developmental and genetic variation. Paired alongside other key metadata, such as strain and
554 sex, MusMorph provides the community with a unique opportunity to disentangle the mechanistic basis for
555 morphological variation.

556 While sparse landmarks are invaluable for geometric morphometrics, there are scenarios where
557 local shape change can be poorly represented. More ambiguous anatomy, such as curves and surfaces,
558 cannot be sufficiently captured with fixed anatomical landmarks, and semi-landmarking each specimen can
559 be tedious and error-prone. Our standardized sparse and dense landmark datasets can enable global and
560 local shape analyses^{102,103}, an area in geometric morphometrics historically overlooked. Homologous dense
561 landmark patches across the embryo datasets will also permit joint superimposition of multiple stages into
562 a common shape space for increased statistical power as well as analyses of ontogeny (Fig. S4). In addition
563 to landmarks, we make the corresponding deformation fields available on an ad hoc basis to support voxel-
564 based meta-analyses of morphology. Despite its ubiquitous application in neuroimaging, voxel-based
565 morphometry is rarely seen in fields that study hard tissue, such as evolutionary developmental biology,
566 anthropology, and paleontology. These deformation fields will let one examine internal and external tissue
567 interactions within anatomical context. Finally, we include anatomical segmentations for several stages,

568 which can be used to restrict the dimensionality of a voxel-wise analysis, calculate the size (e.g., volume or
569 surface area) of a structure, or perform a surface-based morphometry analysis. If users are dissatisfied with
570 the coverage of existing landmarks and segmentations, they can modify the atlases and use the image
571 transformations to generate new labels.

572 We have made the data and scripts freely available at FaceBase (www.facebase.org,
573 doi.org/10.25550/3-HXMC)³⁵ and GitHub (<https://github.com/jaydevine/MusMorph>) to promote
574 transparency, reproducibility, and future data aggregation. Completely open-source efforts like MusMorph
575 are critical for standardizing phenotypic datasets. Unlike the field of genomics, which has been
576 revolutionized through standardized sequencing and data crowdsourcing, phenomics continues to be limited
577 by one-off, self-contained studies that cannot be related to one another. Standardized morphological
578 datasets will allow research groups to, for instance, investigate the effects of a gene mutation alongside
579 other mutants or wildtype strains in a common morphospace. The same can be said for other significant
580 morphological factors and covariates, such as sex and age. Common morphospaces will further encourage
581 multimodal data integration across the phenomic hierarchy, ranging from cellular and developmental
582 phenotyping with light sheet microscopy¹⁰⁴ to tissue phenotyping with magnetic resonance imaging and
583 contrast-enhanced computed tomography³⁸. Large phenotypic datasets will ultimately give us the statistical
584 power needed to interrogate mechanisms that bias and generate morphological variation.

585 *Sources of error and potential limitations*

586 Staining artifacts are a drawback of contrast-enhanced computed tomography. Among the largest sources
587 of registration error were poor contrast and background noise, particularly in the E15.5 dataset. Variable
588 strain penetrance and inadequate contrast can underrepresent anatomy, whereas background noise can
589 masquerade as anatomy and deceive the registration, even if the alignment is constrained with a mask. We
590 mitigated labelling errors by registering thresholded images and by employing other preprocessing
591 techniques, such as intensity bias correction and normalization. However, in some cases, the intensities of

592 the scanning tube could not be distinguished from the specimen, leading to surface landmark errors. Another
593 spatial alignment problem that was difficult to reconcile was variation in articulated anatomical positions.
594 For example, head orientation relative to the body varied widely among the E15.5 and E18.5 datasets, and
595 mandible orientation relative to the skull differed across the adult dataset. We chose to register the entire
596 scan instead of separate segmentations, masks or cropped volumes, because a) a single registration field is
597 computationally more feasible to generate, store, and use downstream and b) a single atlas with a detailed
598 set of labels is better for data standardization.

599 Non-linear alignment and labelling errors may occur around extreme anatomical points with high
600 variability. To demonstrate how automated landmark error can be reduced, we implemented a neural
601 network that minimized automated and manual craniofacial shape differences. Since the endocast,
602 mandible, and embryo datasets do not have manual landmark training data, they cannot be optimized.
603 However, if other investigators have training data, a network could be built to correct sparse phenotyping
604 errors in areas of high morphological variability. Lastly, it is important to consider the computational time
605 and memory needed for volumetric registration. To integrate new data, we strongly encourage users to
606 parallelize their work on compute clusters.

607 *Future development*

608 The majority of MusMorph is composed of head data, because we had reservations about registering whole
609 body data. Now that we have observed no significant differences in registration quality among the datasets,
610 we plan to experiment with more whole-body data for embryos and adults. Another area we intend to
611 improve is our developmental coverage. Despite sampling across most of development, we recognize that
612 additional embryo timepoints (e.g., E9.5 and E12.5-14.5) are needed, as are higher sample sizes throughout
613 mid-gestation and early adulthood. The developing mouse craniofacial complex, for example, undergoes
614 immense growth during the first 30 days after birth¹⁰⁵. Early postnatal datasets will be critical for asking
615 questions about size and ontogenetic allometry. Finally, to complement our large sample of homozygous

616 embryo mutants, we hope to introduce more wildtype and heterozygous embryos for analyses of normal
617 variation. Heterozygotes have not been a focus of the IMPC, so there is ample opportunity to reveal
618 previously unrecognized embryo phenotypes with standardized MusMorph comparisons. The adult dataset,
619 by contrast, needs to be balanced with more homozygous mutants to better understand how mutations of
620 large effect influence morphological variance and other related phenomena, such as integration and
621 modularity.

622 **Usage Notes**

623 MusMorph is categorized as a “Project” on FaceBase. Projects can be found in the “Data Browser: Projects”
624 tab at the top of the home page. Project data are organized hierarchically. The levels of the hierarchy in
625 ascending order of data specificity are “Project”, “Dataset”, “Experiment”, and “Biosample”. A project
626 contains datasets, which are sets of similar studies. Each dataset is annotated with study abstracts,
627 experimental designs, and metadata identifiers. Datasets are composed of experiments. An experiment
628 represents a set of similar specimens, so mice with the same genetic background, age, treatment, and
629 mutation would constitute one experiment. Experiments contain biosamples. A biosample is an individual
630 specimen.

631 After creating a free account and logging in the MusMorph data and metadata can be downloaded
632 at any level in the project hierarchy using the “Export: BDBag” tool at the top-right of the browser. This
633 export function uses DERIVA¹⁰⁶, the software platform that powers FaceBase, to generate a BDBag (Big
634 Data Bag)¹⁰⁷ ZIP file. Users then need to download the file and process it via BDBag client tools, either via
635 the command line or GUI application. Specific details about the DERIVA Client installation and the step-
636 by-step export instructions are available here: www.facebase.org/help/exporting.

637 **Code Availability**

638 Our code is freely available at <https://github.com/jaydevine/MusMorph>. The scripts describe every stage of
639 the MusMorph data acquisition and analysis, including image preprocessing (e.g., file conversion, image
640 resampling and intensity correction), processing (e.g., atlas generation, non-linear registration, label
641 propagation), and postprocessing (e.g., shape optimization, morphometric analysis). We developed and
642 implemented the code with Bash 4.4.20, R 3.6.1, Python 3.6, and Julia 1.2.0 on Ubuntu. All code is
643 distributed under the GNU General Public License v3.0.

644 **Acknowledgements**

645 We thank the Advanced Research Computing team at the University of Calgary for facilitating image
646 processing and storage on the ARC and Helix compute clusters. We also thank FaceBase and the
647 International Mouse Phenotyping Consortium for assisting with image data storage and acquisition. Finally,
648 we would like to acknowledge funding from a CIHR Foundation Grant (#159920), an NSERC Discovery
649 Grant (#238992-17), an NIH R01 (#2R01DE019638), an NIH U01 (#U01DE028729), Alberta Innovates,
650 and the Alberta Children's Hospital Research Institute.

651 **Author contributions**

652 J.D., M.V.G., and B.H.: Study design, image processing, data collection, data analysis, drafting the
653 manuscript, and revising it critically. H.W. and R.S.M.: Study design, data collection, drafting the
654 manuscript, and revising it critically. W.L., A.N., and L.D.L.: Image processing, data collection, and
655 revising the manuscript critically. R.E.S and A.B.: Data upload and organization. R.M.G., H.A.R., M.M.,
656 C.M.U., A.C.N., N.M.Y., P.N.G., C.R., C.J.P., T.W., L.N., A.L.C., A.D.L., A.V., F.R.J., J.M.C., O.K.,
657 R.Y.B., A.E.M., R.R.A., D.G., W.D., B.R., M.H., and S.A.M.: Data collection and revising the manuscript
658 critically. All authors gave final approval for publication.

659 **Competing interests**

660 The authors declare no competing interests.

661 **References**

- 662 1. Hallgrímsson, B., Mio, W., Marcucio, R.S. & Spritz, R. Let's face it—complex traits are just not
663 that simple. *PLoS Genet* **10**, e1004724, <https://doi.org/10.1371/journal.pgen.1004724> (2014).
- 664 2. Mitteroecker, P., Cheverud, J. M. & Pavlicev, M. Multivariate analysis of genotype-phenotype
665 association. *Genetics* **202**, 1345—1363, <https://doi.org/10.1534/genetics.115.181339> (2016).
- 666 3. Pavlicev, M., Norgard, E. A., Fawcett, G. L. & Cheverud, J. M. Evolution of pleiotropy: epistatic
667 interaction pattern supports a mechanistic model underlying variation in genotype-phenotype
668 map. *J. Exp. Zool. (Mol. Dev. Evol.)* **316**, 371—385, <https://doi.org/10.1002/jez.b.21410> (2011).
- 669 4. Green, R. M. *et al.* Developmental nonlinearity drives phenotypic robustness. *Nat. Commun.* **8**,
670 1—12, <https://doi.org/10.1038/s41467-017-02037-7> (2017).
- 671 5. Young, N. M., Chong, H. J., Du, H., Hallgrímsson, B. & Marcucio, R. S. Quantitative analyses
672 link modulation of sonic hedgehog signaling to continuous variation in facial growth and shape.
673 *Development* **137**, 3405—3409, <https://doi.org/10.1242/dev.052340> (2010).
- 674 6. Wagner, G. P. Evolution of gene networks by gene duplications: a mathematical model and its
675 implications on genome organization. *Proc. Natl. Acad. Sci. U. S. A.* **91**, 4387—4391,
676 <https://doi.org/10.1073/pnas.91.10.4387> (1994).
- 677 7. Wagner, G. P. & Zhang, J. The pleiotropic structure of the genotype–phenotype map: the
678 evolvability of complex organisms. *Nat. Rev. Genet.* **12**, 204—213,
679 <https://doi.org/10.1038/nrg2949> (2011).
- 680 8. Rice, S. H. The evolution of canalization and the breaking of von Baer's laws: modeling the
681 evolution of development with epistasis. *Evolution* **52**, 647—656, [https://doi.org/10.1111/j.1558-5646.1998.tb03690.x](https://doi.org/10.1111/j.1558-
682 5646.1998.tb03690.x) (1998).
- 683 9. Rice, S. H. Theoretical approaches to the evolution of development and genetic architecture. *Ann.
684 N.Y. Acad. Sci.* **1133**, 67—86, <https://doi.org/10.1196/annals.1438.002> (2008).
- 685 10. Hallgrímsson, B. *et al.* The developmental-genetics of canalization. In *Seminars in Cell &
686 Developmental Biology*, Vol. 88 (Academic Press, 2019).
687 <https://doi.org/10.1016/j.semcd.2018.05.019>.
- 688 11. Karim, K. *et al.* Xenbase: a genomic, epigenomic and transcriptomic model organism database.
689 *Nucleic Acids Res.* **46**, D861—D868, <https://doi.org/10.1093/nar/gkx936> (2018).
- 690 12. Blake, J. A. *et al.* The Mouse Genome Database (MGD): the model organism database for the
691 laboratory mouse. *Nucleic Acids Res.* **30**, 113—115, <https://doi.org/10.1093/nar/30.1.113> (2002).
- 692 13. Howe *et al.* ZFIN, the Zebrafish Model Organism Database: increased support for mutants and
693 transgenics. *Nucleic Acids Res.* **41**, D854—D860, <https://doi.org/10.1093/nar/gks938> (2012).
- 694 14. Wang, L., Wang, S., Li, Y., Paradesi, M. S. R. & Brown, S. J. BeetleBase: the model organism
695 database for *Tribolium castaneum*. *Nucleic Acids Res.* **35**, D476—D479,
696 <https://doi.org/10.1093/nar/gkl776> (2006).
- 697 15. Brown, S. D. & Moore, M. W. The International Mouse Phenotyping Consortium: past and future
698 perspectives on mouse phenotyping. *Mamm. Genome* **23**, 632—640,
699 <https://doi.org/10.1007/s00335-012-9427-x> (2012).
- 700 16. Brown, S. D. & Moore, M. W. Towards an encyclopaedia of mammalian gene function: The
701 International Mouse Phenotyping Consortium. *Dis. Model. Mech.* **5**, 289—292,
702 <https://doi.org/10.1242/dmm.009878> (2012).
- 703 17. Horner, N. R. *et al.* LAMA: automated image analysis for the developmental phenotyping of
704 mouse embryos. *Development* **148**, dev192955, <https://doi.org/10.1242/dev.192955> (2021).

705 18. Koscielny, G. *et al.* The International Mouse Phenotyping Consortium Web Portal, a unified
706 point of access for knockout mice and related phenotyping data. *Nucleic Acids Res.* **42**, D802—
707 D809, <https://doi.org/10.1093/nar/gkt977> (2014).

708 19. Meehan, T. F. *et al.* Disease model discovery from 3,328 gene knockouts by The International
709 Mouse Phenotyping Consortium. *Nat. Genet.* **49**, 1231—1238, <https://doi.org/10.1038/ng.3901>
710 (2017).

711 20. Dickinson, M. E. *et al.* High-throughput discovery of novel developmental phenotypes. *Nature*
712 **537**, 508—514, <https://doi.org/10.1038/nature19356> (2016).

713 21. Churchill, G. A., Gatti, D. M., Munger, S. C. & Svenson, K. L. The diversity outbred mouse
714 population. *Mamm. Genome* **23**, 713—718, <https://doi.org/10.1007/s00335-012-9414-2> (2012).

715 22. Collaborative Cross Consortium. The genome architecture of the Collaborative Cross mouse
716 genetic reference population. *Genetics* **190**, 389—401,
717 <https://doi.org/10.1534/genetics.111.132639> (2012).

718 23. Katz, D. C. *et al.* Facial shape and allometry quantitative trait locus intervals in the Diversity
719 Outbred mouse are enriched for known skeletal and facial development genes. *PLoS ONE* **15**,
720 e023337, <https://doi.org/10.1371/journal.pone.0233377> (2020).

721 24. Ashburner, J. & Friston, K. J. Voxel-based morphometry—the methods. *NeuroImage* **11**, 805—
722 821, <https://doi.org/10.1006/nimg.2000.0582> (2000).

723 25. Fonov, V. *et al.* Unbiased average age-appropriate atlases for pediatric studies. *NeuroImage* **54**,
724 313—327, <https://doi.org/10.1016/j.neuroimage.2010.07.033> (2011).

725 26. Ridgway, G. R. *et al.* Ten simple rules for reporting voxel-based morphometry studies.
726 *NeuroImage* **40**, 1429—1435, <https://doi.org/10.1016/j.neuroimage.2008.01.003> (2008).

727 27. Silver, M., Montana, G., Nichols, T. E. & Alzheimer's Disease Neuroimaging Initiative. False
728 positives in neuroimaging genetics using voxel-based morphometry data. *NeuroImage* **54**, 992—
729 1000, <https://doi.org/10.1016/j.neuroimage.2010.08.049> (2011).

730 28. Adams, D. C., Rohlf, F. J. & Slice, D. E. A field comes of age: geometric morphometrics in the
731 21st century. *Hystrix* **24**, 7, <https://doi.org/10.4404/hystrix-24.1-6283> (2013).

732 29. Boyer, D. M. *et al.* A new fully automated approach for aligning and comparing shapes. *Anat.*
733 *Rec.* **298**, 249—276, <https://doi.org/10.1002/ar.23084> (2015).

734 30. Maga, A. M., Tustison, N. J. & Avants, B. B. A population level atlas of *Mus musculus*
735 craniofacial skeleton and automated image-based shape analysis. *J. Anat.* **231**, 433—443,
736 <https://doi.org/10.1111/joa.12645> (2017).

737 31. Porto, A. & Voje, K. L. ML-morph: A fast, accurate and general approach for automated
738 detection and landmarking of biological structures in images. *Methods Ecol. Evol.* **11**, 500—512,
739 <https://doi.org/10.1111/2041-210X.13373> (2020).

740 32. Rolfe, S. *et al.* SlicerMorph: An open and extensible platform to retrieve, visualize and analyze
741 3D morphology. *bioRxiv*, <https://doi.org/10.1101/2020.11.09.374926> (2020).

742 33. Vidal-García, M., Bandara, L. & Keogh, J. S. ShapeRotator: an R tool for standardized rigid
743 rotations of articulated three-dimensional structures with application for geometric
744 morphometrics. *Ecol. Evol.* **8**, 4669—4675, <https://doi.org/10.1002/ece3.4018> (2018).

745 34. Samuels, B. D. *et al.* FaceBase 3: analytical tools and FAIR resources for craniofacial and dental
746 research. *Development* **147**, dev191213, <https://doi.org/10.1242/dev.191213> (2020).

747 35. Devine, J. *et al.* MusMorph, a database of standardized mouse morphology data for
748 morphometric meta-analyses. *FaceBase Consortium*, <https://doi.org/10.25550/3-HXMC> (2021).

749 36. Devine, J. *et al.* Project-wide metadata, atlases, and landmarks for MusMorph. *FaceBase*
750 *Consortium*, <https://doi.org/10.25550/6-2EPY> (2021).

751 37. Wong, M. D., Spring, S. & Henkelman, R. M. Structural stabilization of tissue for embryo
752 phenotyping using micro-CT with iodine staining. *PLoS ONE* **8**, e84321,
753 <https://doi.org/10.1371/journal.pone.0084321> (2013).

754 38. Gignac, P. M. *et al.* Diffusible iodine-based contrast-enhanced computed tomography (diceCT):
755 an emerging tool for rapid, high-resolution, 3-D imaging of metazoan soft tissues. *J. Anat.* **228**,
756 889—909, <https://doi.org/10.1111/joa.12449> (2016).

757 39. Green, R. M., Leach, C. L., Hoehn, N., Marcucio, R. S. & Hallgrímsson, B. Quantifying three-
758 dimensional morphology and RNA from individual embryos. *Dev. Dynam.* **246**, 431—436,
759 <https://doi.org/10.1002/DVDY.24490> (2017).

760 40. Feldkamp, L. A., Davis, L. C. & Kress, J. W. Practical cone-beam algorithm. *J. Opt. Soc. Am. A*
761 **1**, 612—619, <https://doi.org/10.1364/JOSAA.1.0000612> (1984).

762 41. Vincent, R. D. *et al.* MINC 2.0: a flexible format for multi-modal images. *Front. Neuroinform.*
763 **10**, 35, <https://doi.org/10.3389/fninf.2016.00035> (2016).

764 42. Sled, J. G., Zijdenbos, A. P. & Evans, A. C. A nonparametric method for automatic correction of
765 intensity nonuniformity in MRI data. *IEEE T. Med. Imaging* **17**, 87—97,
766 <https://doi.org/10.1109/42.668698> (1998).

767 43. Friedel, M., van Eede, M. C., Pipitone, J., Chakravarty, M. M. & Lerch, J. P. Pydpiper: a flexible
768 toolkit for constructing novel registration pipelines. *Front. Neuroinform.* **8**, 67,
769 <https://doi.org/10.3389/fninf.2014.00067> (2014).

770 44. Percival, C. J. *et al.* The effect of automated landmark identification on morphometric analyses. *J.*
771 *Anat.* **234**, 917—935, <https://doi.org/10.1111/joa.12973> (2019).

772 45. Collins, D. L., Neelin, P., Peters, T. M. & Evans, A. C. Automatic 3D intersubject registration of
773 MR volumetric data in standardized Talairach space. *J. Comput. Assist. Tomo.* **18**, 192—205,
774 <https://doi.org/10.1097/00004728-199403000-00005> (1994).

775 46. Lerch, J. P., Sled, J. G. & Henkelman, R. M. MRI Phenotyping of Genetically Altered Mice. In:
776 *Magnetic Resonance Neuroimaging*. Methods in Molecular Biology (Methods and Protocols),
777 Vol. 711 (eds. Modo M., Bulte, J.) (Humana Press, 2011). https://doi.org/10.1007/978-1-61737-992-5_17.

779 47. Collins, D. L. & Evans, A. C. Animal: validation and applications of nonlinear registration-based
780 segmentation. *Int. J. Pattern Recogn.* **11**, 1271—1294,
781 <https://doi.org/10.1142/S0218001497000597> (1997).

782 48. Wong, M. D., Dorr, A. E., Walls, J. R., Lerch, J. P. & Henkelman, R. M. A novel 3D mouse
783 embryo atlas based on micro-CT. *Development* **139**, 3248—3256,
784 <https://doi.org/10.1242/dev.082016> (2012).

785 49. Kikinis R., Pieper S. D. & Vosburgh K. G. 3D Slicer: A Platform for Subject-Specific Image
786 Analysis, Visualization, and Clinical Support. In: *Intraoperative Imaging and Image-Guided*
787 *Therapy* (eds. Jolesz, F.) (Springer, 2014). https://doi.org/10.1007/978-1-4614-7657-3_19.

788 50. Percival, C. J., Green, R., Marcucio, R. S. & Hallgrímsson, B. Surface landmark quantification of
789 embryonic mouse craniofacial morphogenesis. *BMC Dev. Biol.* **14**, 1—12,
790 <https://doi.org/10.1186/1471-213X-14-31> (2014).

791 51. Bastir, M. A systems-model for the morphological analysis of integration and modularity in
792 human craniofacial evolution. *J. Anthropol. Sci.* **86**, 19934468 (2008).

793 52. Porto, A., de Oliveira F. B., Shirai, L. T., De Conto, V. & Marroig, G. The evolution of
794 modularity in the mammalian skull I: Morphological integration patterns and magnitudes. *Evol.*
795 *Biol.* **36**, 118—135, <https://doi.org/10.1007/s11692-008-9038-3> (2009).

796 53. Hallgrímsson, B. *et al.* Integration and the developmental genetics of allometry. *Integr. Comp.*
797 *Biol.* **59**, 1369—1381, <https://doi.org/10.1093/icb/icz105> (2019).

798 54. Richtsmeier, J. T. *et al.* Phenotypic integration of neurocranium and brain. *J. Exp. Zool. (Mol.*
799 *Dev. Evol.)* **306**, 360—378, <https://doi.org/10.1002/jez.b.21092> (2006).

800 55. Marchini, M. *et al.* Wnt signaling drives correlated changes in facial morphology and brain shape.
801 *Front. Cell Dev. Biol.* **9**, 694, <https://doi.org/10.3389/fcell.2021.644099> (2021).

802 56. Smith, K. K. Integration of craniofacial structures during development in mammals. *Am. Zool.* **36**,
803 70—79 (1996).

804 57. Young, N. M., Linde-Medina, M., Fondon, J. W., Hallgrímsson, B. & Marcucio, R. S.
805 Craniofacial diversification in the domestic pigeon and the evolution of the avian skull. *Nat. Ecol.*
806 *Evol.* **1**, 1—8, <https://doi.org/10.1038/s41559-017-0095> (2017).

807 58. Toussaint, N. *et al.* A landmark-free morphometrics pipeline for high-resolution phenotyping:
808 application to a mouse model of Down syndrome. *Development* **148**, dev188631,
809 <https://doi.org/10.1242/dev.188631> (2021).

810 59. Avants, B. B. *et al.* A reproducible evaluation of ANTs similarity metric performance in brain
811 image registration. *NeuroImage* **54**, 2033—2044,
812 <https://doi.org/10.1016/j.neuroimage.2010.09.025> (2011).

813 60. Devine, J. *et al.* A registration and deep learning approach to automated landmark detection for
814 geometric morphometrics. *Evol. Biol.* **47**, 246—259, <https://doi.org/10.1007/s11692-020-09508-8>
815 (2020).

816 61. Attanasio, C. *et al.* Fine tuning of craniofacial morphology by distant-acting enhancers. *Science*
817 **342**, 1—20, <https://doi.org/10.1126/science.1241006> (2014).

818 62. Hallgrímsson, B., Willmore, K., Dorval, C. & Cooper, D. M. L. Craniofacial variability and
819 modularity in macaques and mice. *J. Exp. Zool. Part B* **302**, 207—225,
820 <https://doi.org/10.1002/jez.b.21002> (2004).

821 63. Hallgrímsson, B. *et al.* The Brachymorph mouse and the developmental-genetic basis for
822 canalization and morphological integration. *Evol. Dev.* **8**, 61—73, <https://doi.org/10.1111/j.1525-142X.2006.05075.x> (2006).

824 64. Hallgrímsson, B. *et al.* Deciphering the Palimpsest: Studying the relationship between
825 morphological integration and phenotypic covariation. *Evol. Biol.* **36**, 355—376,
826 <https://doi.org/10.1007/s11692-009-9076-5> (2009).

827 65. Lieberman, D. E., Hallgrímsson, B., Liu, W., Parsons, T. E. & Jamniczky, H. A. Spatial packing,
828 cranial base angulation, and craniofacial shape variation in the mammalian skull: Testing a new
829 model using mice. *J. Anat.* **212**, 720—735, <https://doi.org/10.1111/j.1469-7580.2008.00900.x>
830 (2008).

831 66. Devine, J. *et al.* Collaborative Cross: A standardized mouse morphology dataset for MusMorph.
832 *FaceBase Consortium*, <https://doi.org/10.25550/3-KB0W> (2021).

833 67. Devine, J. *et al.* Hybrid: A standardized mouse morphology dataset for MusMorph. *FaceBase*
834 *Consortium*, <https://doi.org/10.25550/3-KB32> (2021).

835 68. Devine, J. *et al.* Diversity Outbred: A standardized mouse morphology dataset for MusMorph.
836 *FaceBase Consortium*, <https://doi.org/10.25550/3-KB0W> (2021).

837 69. Devine, J. *et al.* IMPC: A standardized mouse morphology dataset for MusMorph. *FaceBase*
838 *Consortium*, <https://doi.org/10.25550/3-JZA6> (2021).

839 70. Devine, J. *et al.* Ap2: A standardized mouse morphology dataset for MusMorph. *FaceBase*
840 *Consortium*, <https://doi.org/10.25550/3-JQMG> (2021).

841 71. Devine, J. *et al.* B9d: A standardized mouse morphology dataset for MusMorph. *FaceBase*
842 *Consortium*, <https://doi.org/10.25550/3-JQMM> (2021).

843 72. Devine, J. *et al.* Bulgy: A standardized mouse morphology dataset for MusMorph. *FaceBase*
844 *Consortium*, <https://doi.org/10.25550/3-JZ9G> (2021).

845 73. Devine, J. *et al.* Brain-Face: A standardized mouse morphology dataset for MusMorph. *FaceBase*
846 *Consortium*, <https://doi.org/10.25550/3-KB3J> (2021).

847 74. Devine, J. *et al.* Longshanks: A standardized mouse morphology dataset for MusMorph.
848 *FaceBase Consortium*, <https://doi.org/10.25550/3-KFBE> (2021).

849 75. Unger, C. M., Devine, J., Hallgrímsson, B. & Rolian, C. Selection for increased tibia length in
850 mice alters skull shape through parallel changes in developmental mechanisms. *Elife* **10**, e67612,
851 <https://doi.org/10.7554/eLife.67612> (2021).

852 76. Marchini, M. & Rolian, C. Artificial selection sheds light on developmental mechanisms of limb
853 elongation. *Evolution* **72**, 825—837, <https://doi.org/10.1111/evo.13447> (2018).

854 77. Spring, S., Lerch, J. P. & Henkelman, R. M. Sexual dimorphism revealed in the structure of the
855 mouse brain using three-dimensional magnetic resonance imaging. *NeuroImage* **35**, 1424—1433,
856 <https://doi.org/10.1016/j.neuroimage.2007.02.023> (2007).

857 78. Gonzalez, P. N., Bernal, V. & Perez, S. I. Analysis of sexual dimorphism of craniofacial traits
858 using geometric morphometric techniques. *Int. J. Osteoarchaeol.* **21**, 82—91,
859 <https://doi.org/10.1002/oa.1109> (2011).

860 79. Callewaert, F. *et al.* Sexual dimorphism in cortical bone size and strength but not density is
861 determined by independent and time-specific actions of sex steroids and IGF-1: Evidence from
862 pubertal mouse models. *J. Bone Miner. Res.* **25**, 617—626, <https://doi.org/10.1359/jbmr.090828>
863 (2010).

864 80. Grove, K. L., Fried, S. K., Greenberg, A. S., Xiao, X. Q. & Clegg, D. J. A microarray analysis of
865 sexual dimorphism of adipose tissues in high-fat-diet-induced obese mice. *Int. J. Obesity* **34**,
866 989—1000, <https://doi.org/10.1038/ijo.2010.12> (2010).

867 81. Eaton, M. *et al.* Complex patterns of cell growth in the placenta in normal pregnancy and as
868 adaptations to maternal diet restriction. *PLoS ONE* **15**, e0226735,
869 <https://doi.org/10.1371/journal.pone.0226735> (2020).

870 82. Gonzalez *et al.* Chronic protein restriction in mice impacts placental function and maternal body
871 weight before fetal growth. *PLoS ONE* **11**, e0152227,
872 <https://doi.org/10.1371/journal.pone.0152227> (2016).

873 83. Devine, J. *et al.* Strain Comparison: A standardized mouse morphology dataset for MusMorph.
874 *FaceBase Consortium*, <https://doi.org/10.25550/3-JZ9J> (2021).

875 84. Jamniczky, H. A. & Hallgrímsson, B. A comparison of covariance structure in wild and
876 laboratory muroid crania. *Evolution* **63**, 1540—1556, <https://doi.org/10.1111/j.1558-5646.2009.00651.x> (2009).

877 85. Davies, A. G., Bettinger, J. C., Thiele, T. R., Judy, M. E. & McIntire, S. L. Natural variation in
878 the npr-1 gene modifies ethanol responses of wild strains of *C. elegans*. *Neuron* **42**, 731—743,
879 <https://doi.org/10.1016/j.neuron.2004.05.004> (2004).

880 86. Pavlicev, M., Norgard, E. A., Fawcett, G. L. & Cheverud, J. M. Evolution of pleiotropy: epistatic
881 interaction pattern supports a mechanistic model underlying variation in genotype–phenotype
882 map. *J. Exp. Zool. (Mol. Dev. Evol.)* **316**, 371—385 (2011).

883 87. Percival, C. J., Marangoni, P., Tapaltsyan, V., Klein, O. & Hallgrímsson, B. The interaction of
884 genetic background and mutational effects in regulation of mouse craniofacial shape. *G3—Genes*
885 *Genom. Genet.* **7**, 1439—1450, <https://doi.org/10.1534/g3.117.040659> (2017).

886 88. Devine, J. *et al.* Spry: A standardized mouse morphology dataset for MusMorph. *FaceBase*
887 *Consortium*, <https://doi.org/10.25550/3-JZAM> (2021).

888 89. Cheverud, J. M. Relationships among ontogenetic, static, and evolutionary allometry. *Am. J.*
889 *Phys. Anthropol.* **59**, 139—149 (1982).

890

891 90. Gonzalez, P. N., Kristensen, E., Morck, D. W., Boyd, S. & Hallgrímsson, B. Effects of growth
892 hormone on the ontogenetic allometry of craniofacial bones. *Evol. Dev.* **15**, 133—145,
893 <https://doi.org/10.1111/ede.12025> (2013).

894 91. Klingenberg, C. P. Multivariate allometry. In *Advances in Morphometrics* (Springer, 1996).
895 https://doi.org/10.1007/978-1-4757-9083-2_3.

896 92. Mosimann, J. E. Size allometry: size and shape variables with characterizations of the lognormal
897 and generalized gamma distributions. *J. Am. Stat. Assoc.* **65**, 930—945,
898 <https://doi.org/10.1080/01621459.1970.10481136> (1970).

899 93. Jolicoeur, P. Note: the multivariate generalization of the allometry equation. *Biometrics* **19**,
900 497—499, <https://doi.org/10.2307/2527939> (1963).

901 94. Richtsmeier, J. T. & Flaherty, K. Hand in glove: brain and skull in development and
902 dysmorphogenesis. *Acta. Neuropathol.* **125**, 469—489 (2013).

903 95. Klingenberg, C. P. Morphometrics and the role of the phenotype in studies of the evolution of
904 developmental mechanisms. *Gene* **287**, 3—10, [https://doi.org/10.1016/S0378-1119\(01\)00867-8](https://doi.org/10.1016/S0378-1119(01)00867-8)
905 (2002).

906 96. Soulé, M. E. Heterozygosity and developmental stability: another look. *Evolution* **33**, 396—401,
907 <https://doi.org/10.2307/2407629> (1979).

908 97. Sotiras, A., Davatzikos, C. & Paragios, N. Deformable medical image registration: A survey.
909 *IEEE T. Med. Imaging* **32**, 1153—1190, <https://doi.org/10.1109/TMI.2013.2265603> (2013).

910 98. Devine, J. *et al.* Ghrhr: A standardized mouse morphology dataset for MusMorph. *FaceBase
911 Consortium*, <https://doi.org/10.25550/3-KB08> (2021).

912 99. Vidal-García, M. morpho. Tools. GM v1.0.0: A set of R tools to help with geometric
913 morphometric analyses of 3D data. <https://doi.org/10.5281/zenodo.4673771> (2021).

914 100. Wong, M. D. *et al.* 4D atlas of the mouse embryo for precise morphological staging.
915 *Development* **142**, 3583—3591, <https://doi.org/10.1242/dev.125872> (2015).

916 101. Schlager, S. Morpho and Rvcg—Shape analysis in R: R packages for geometric morphometrics,
917 shape analysis and surface manipulations. In *Statistical Shape and Deformation Analysis.
918 Methods, Implementation and Applications* (Academic Press, 2017).
919 <https://doi.org/10.1016/B978-0-12-810493-4.00011-0>.

920 102. Claes, P. *et al.* Genome-wide mapping of global-to-local genetic effects on human facial shape.
921 *Nat. Genet.* **50**, 414—423, <https://doi.org/10.1038/s41588-018-0057-4> (2018).

922 103. Mitteroecker, P. *et al.* Morphometric variation at different spatial scales: coordination and
923 compensation in the emergence of organismal form. *Syst. Biol.* **69**, 913—926,
924 <https://doi.org/10.1093/sysbio/syaa007> (2020).

925 104. Epp, J. R. *et al.* Optimization of CLARITY for clearing whole-brain and other intact organs.
926 *eNeuro* **2**, <https://doi.org/10.1523/ENEURO.0022-15.2015> (2015).

927 105. Vora, S. R., Camci E. D. & Cox, T. C. Postnatal ontogeny of the cranial base and craniofacial
928 skeleton in male C57BL/6J mice: A reference standard for quantitative analysis. *Front. Physiol.*
929 **6**, 417, <https://doi.org/10.3389/fphys.2015.00417> (2016).

930 106. Bugacov, A. *et al.* Experiences with DERIVA: An asset management platform for accelerating
931 eScience. In: *IEEE 13th International Conference on e-Science*, 79—88,
932 <https://doi.org/10.1109/eScience.2017.20> (2017).

933 107. Chard, K. *et al.* I'll take that to go: Big data bags and minimal identifiers for exchange of large,
934 complex datasets. In: *IEEE International Conference on Big Data*, 319—328,
935 <https://doi.org/10.1109/BigData.2016.7840618> (2016).

936